Wensi Wu
Department of Anesthesiology
and Critical Care Medicine,
Children's Hospital of Philadelphia,
Philadelphia, PA 19104

Stephen Ching
Department of Anesthesiology
and Critical Care Medicine,
Children's Hospital of Philadelphia,
Philadelphia, PA 19104

Steve A. Maas
Department of Biomedical Engineering,
Scientific Computing and Imaging Institute,
University of Utah,
Salt Lake City, UT 84112

Andras Lasso
Laboratory for Percutaneous Surgery,
Queen's University,
Kingston, ON K7L 3N6, Canada

Patricia Sabin
Department of Anesthesiology
and Critical Care Medicine,
Children's Hospital of Philadelphia,
Philadelphia, PA 19104

Jeffrey A. Weiss
Department of Biomedical Engineering,
Scientific Computing and Imaging Institute,
University of Utah,
Salt Lake City, UT 84112

Matthew A. Jolley[1]
Department of Anesthesiology
and Critical Care Medicine,
Division of Pediatric Cardiology,
Children's Hospital of Philadelphia,
Philadelphia, PA 19104

A Computational Framework for Atrioventricular Valve Modeling Using Open-Source Software

Atrioventricular valve regurgitation is a significant cause of morbidity and mortality in patients with acquired and congenital cardiac valve disease. Image-derived computational modeling of atrioventricular valves has advanced substantially over the last decade and holds particular promise to inform valve repair in small and heterogeneous populations, which are less likely to be optimized through empiric clinical application. While an abundance of computational biomechanics studies has investigated mitral and tricuspid valve disease in adults, few studies have investigated its application to vulnerable pediatric and congenital heart populations. Further, to date, investigators have primarily relied upon a series of commercial applications that are neither designed for image-derived modeling of cardiac valves nor freely available to facilitate transparent and reproducible valve science. To address this deficiency, we aimed to build an open-source computational framework for the image-derived biomechanical analysis of atrioventricular valves. In the present work, we integrated an open-source valve modeling platform, SlicerHeart, and an open-source biomechanics finite element modeling software, FEBio, to facilitate image-derived atrioventricular valve model creation and finite element analysis. We present a detailed verification and sensitivity analysis to demonstrate the fidelity of this modeling in application to three-dimensional echocardiography-derived pediatric mitral and tricuspid valve models. Our analyses achieved an excellent agreement with those reported in the literature. As such, this evolving computational framework offers a promising initial foundation for future development and investigation of valve mechanics, in particular collaborative efforts targeting the development of improved repairs for children with congenital heart disease. [DOI: 10.1115/1.4054485]

Keywords: atrioventricular valves, uncertainty analysis, valve mechanics, contact potential, finite element modeling, open-source

1 Introduction

Multimodality imaging, including three-dimensional echocardiography (3DE), has transformed adult mitral valve surgery by capturing the full, complex geometry of the valve in real-time, providing an intuitive view of the functioning valve directly to the surgeon. While informative, three-dimensional (3D) visualization alone is insufficient for quantitative assessment and analysis of the valve. The development of image-derived mitral valve computer modeling tools has partially unlocked this potential, allowing precise, quantitative comparison of normal valves to dysfunctional valves, greatly improving the understanding of the 3D structural correlates of adult mitral valve dysfunction [1–4]. However, correlation cannot infer causality: it does not elucidate the physical basis for why valves fail over time or allow the testing and comparison of novel repair strategies. The application of image-derived finite element (FE) modeling has begun to provide this capability, bringing forth the potential to determine patient-specific structural contributors to valve stress, strain, and failure, as well as the development of the optimal repair for an individual patient [5–10]. Specifically, computational modeling allows for investigations of valve function and assessment of leaflet stress and strain that would otherwise be unobtainable using conventional in vitro methods or clinical trials [9].

Significant advances in FE modeling of the mitral and tricuspid valve have occurred over the last decade [5,9,11–14]. Notably, several barriers to the application of FE analysis to the modeling of atrioventricular valves from human images have been significantly addressed through these studies. Initial FE models were constructed from micro-CT images of ex-vivo animal and cadaveric human hearts. These high-resolution images clearly demonstrated the papillary and chordal support structure for the valve and provided a detailed roadmap for incorporation of those structures into the valve model. However, while valve leaflets and papillary muscle heads are clearly visible in living human 3DE and tomographic imaging, the individual chords are not reliably visualized. Thankfully, Khalighi et al. compared simplified distributed chordal models to "ground truth" models based on micro-CT and showed that for chord density greater than 15 chords/cm^2, the results were functionally equivalent to the ground truth models

[1]Corresponding author.
Manuscript received January 31, 2022; final manuscript received April 27, 2022; published online May 27, 2022. Assoc. Editor: Craig Goergen.

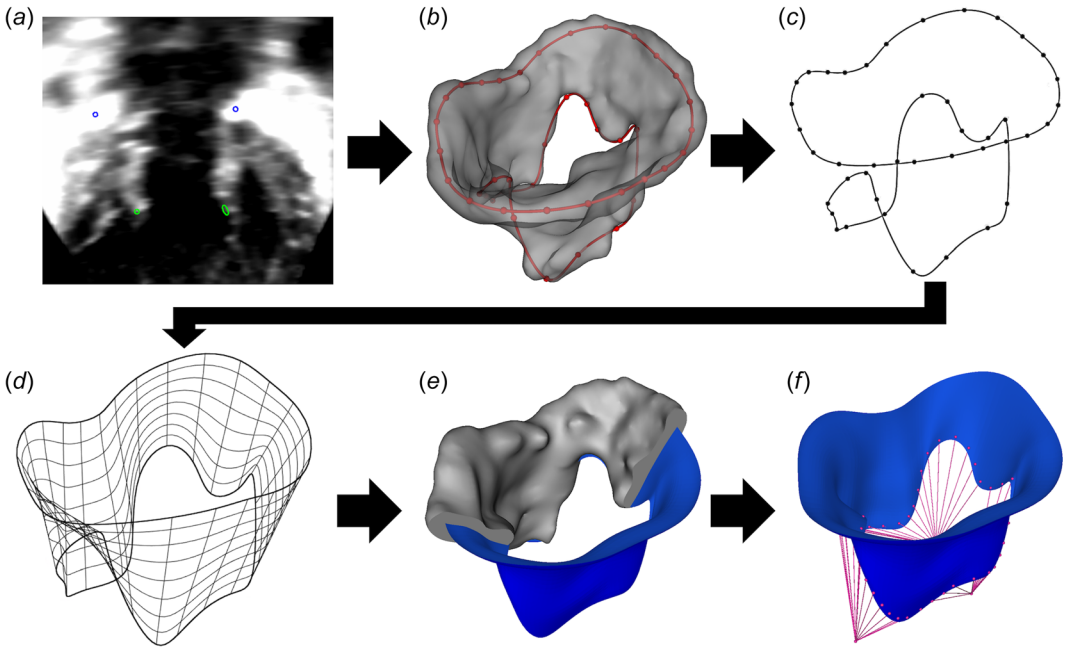

Fig. 1 FE modeling pipeline from 3DE image, demonstrated on tricuspid valve: valve construction process from 3DE image to FE model: (*a*) define annulus and free edge control points (3D Slicer SlicerHeart), (*b*) create leaflet segmentation (SlicerHeart), (*c*) create splines (SlicerHeart), (*d*) initialize Non-Uniform Rational B-Spline (NURBS) surface (Autodesk Fusion 360), (*e*) adjust NURBS surface to segmentation (Fusion 360), and (*f*) project chordae onto leaflets (SlicerHeart). The development of leaflet medial surface extraction and NURBS editing is underway in SlicerHeart to allow all functionality in a single open-source workflow.

[8]. This study opened the potential to utilize living human clinical images as the basis for FE analysis to investigate valve leaflet stress and strain. A second advance has been the development of realistic constitutive models and specialized FE techniques to support the requirements necessary for the modeling of valve biomechanics [9,13,15]. Finally, the complexity associated with modeling thin pliable structures and obtaining stable solutions (convergence) when modeling complex valve leaflet motion has been challenging [11,16]. Kamensky et al. recently described a potential-based contact algorithm that is particularly well suited for valve leaflet modeling and has been subsequently validated for modeling the tricuspid valve [13,17,18]. The combination of these advances brings the field to a state where FE analysis may be meaningfully applied to derived from 3D images of atrioventricular valves in living humans.

Building on this capability, previous investigations have demonstrated that perturbations of valve structure result in differences in leaflet stress and strain in image-derived models of the adult mitral valve, and more recently, the tricuspid valve [9,11–14]. Notably, elevated leaflet stress and strain are associated with valve failure, pathologic changes in valve leaflets (leaflet prolapse, chordal rupture), and changes in valve leaflet gene expression [4,19–23]. Further, FE investigations in the mitral and tricuspid valve have demonstrated how both image-derived and parametric valve models can be "surgically" altered to precisely investigate the effect of anatomic variation and surgical interventions upon leaflet stress, strain, and coaptation [5,9,15,16]. These modeling capabilities may be particularly well suited to the optimization of valve repair techniques in small and heterogeneous populations, such as children with congenital heart disease, who do not benefit from empiric validation of valve repair techniques through high-volume application.

However, the majority of methods described to date leverage serial application of multiple different commercial software platforms that are not fully modifiable or configurable by the end-user. A different commercial tool is used to import 3D data, create models, incorporate models in FE software, and run simulations. Further, each commercial tool is not open or transparent as to its methodology, limiting reproducibility and extension of functionality. Similarly, suitable contact and constitutive models for valve modeling are not typically provided in such packages. As such, there is a need for the development of an open-source pipeline for computational valve modeling to catalyze open and transparent valve science. In a major step toward an integrated image-derived valve modeling pipeline, we implemented a robust constitutive model and a novel contact potential formulation in the FEBio FE software[2], [24–26] and applied it to 3DE image-derived models of pediatric mitral and tricuspid valves. We then performed a detailed sensitivity analysis of the effect of varying modeling parameters upon leaflet stress and strain to verify the newly implemented framework.

2 Methods

In the present work, we integrated and employed open-source platforms to facilitate the computational modeling process: SlicerHeart[3] [27,28], 3D Slicer[4] [29], and FEBio 3.5.1 [24,25,26]. The current pipeline consisted of two major procedures. First, we constructed 3DE-derived FE models of atrioventricular valves using SlicerHeart and 3D Slicer. Second, we imported those valve models and performed FE analyses to assess the mechanical responses of the valves using FEBio. Notably, while we utilized 3DE in this study, this workflow is fundamentally applicable to images created using computed tomography (CT) or cardiac magnetic resonance imaging (MRI).

2.1 Data Import and Valve Model Creation. This study was approved by the Institutional review board at the Children's Hospital of Philadelphia. 3DE of mitral and tricuspid valves were identified from an existing database at the Children's Hospital of Philadelphia. The mitral valve was based on a 15-year-old male

[2]www.febio.org
[3]www.github.com/SlicerHeart
[4]www.slicer.org

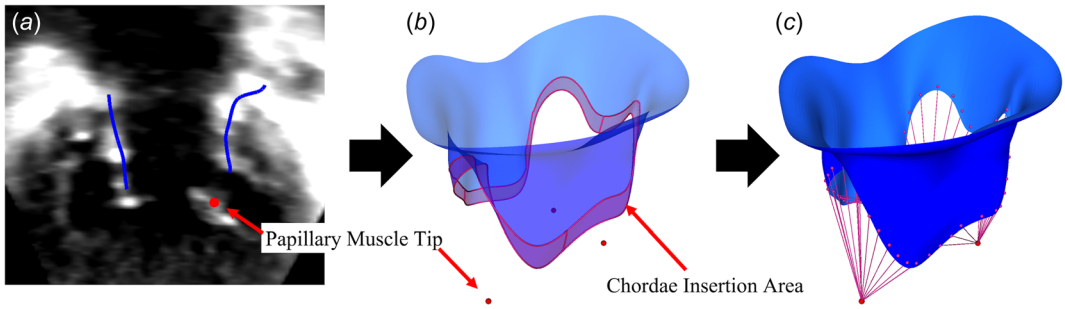

Fig. 2 FE modeling pipeline from 3D echocardiographic image, demonstrated on tricuspid valve: chordae tendineae modeling: (*a*) identify papillary muscles (3D Slicer SlicerHeart), (*b*) define chordal insertion area, indicated here by the shaded region (SlicerHeart), and (*c*) project chordae (SlicerHeart)

with normal heart anatomy and no mitral regurgitation. The tricuspid valve was based on a 3-year-old male with hypoplastic left heart syndrome with no significant valve regurgitation. Images had been acquired on a Philips Epiq system (Philips Medical, Andover, MA). The 3DE volume data (DICOM) were imported into 3D Slicer using the Philips 4D U.S. DICOM patcher module in SlicerHeart, as previously described [27,28].

The valve model creation pipeline is described in Fig. 1. First, the valves were segmented in the Slicer Heart extension in 3D Slicer. The annulus was defined in the desired mid-diastolic frame (i.e., the median time point between the last frame of when the valve is closed and the first frame when the valve is closed in the succeeding cardiac cycle) using the Annulus Analysis module as outlined in Scanlan et al. [28,30]. Subsequently, using the Valve Segmentation module, the leaflets were traced for each slice of the image from the annulus to the free edge. This process was repeated for each slice until the entire diastolic valve has been segmented [27]. The FE models were created by first defining the annular contour curve using a 24-control point periodic spline. A second periodic control point spline was constructed along the free edges of the leaflets to model the valve orifice. The resulting models were imported into Autodesk Fusion 360 (Auto-Desk, San Rafael, CA). A Non-Uniform rational B-Spline (NURBS) surface was then lofted between the two curves to create the leaflets and valve surface. Control points on the NURBS surface were further edited to match the native geometry of the segmentation of the valve. This was the only part of the workflow that is not currently open-source, and the development of leaflet medial surface extraction and NURBS editing is underway in SlicerHeart to eliminate this need.

A custom Python scripted workflow was preliminarily created in SlicerHeart to distribute the chordae evenly along the leaflets (Fig. 2). The chordae tendineae are not reliably identifiable from 3DE images, but the papillary muscle origins can readily be seen. The locations of the papillary muscle tips were identified in the 3DE image within 3D Slicer, and the registered coordinates were used to model the chordal origins as a single point per papillary muscle, as demonstrated by Khaligi et al. [12].

2.2 Constitutive Model of Atrioventricular Valve Leaflets. Atrioventricular valve leaflets consist of three layers of tissue: fibrosa, spongiosa, and atrialis. The fibrosa is the thickest layer of the three, and is directed toward the ventricular chamber, while the atrialis layer, as the name suggests, is directed toward the atria. The fibrosa layer is composed primarily of type I collagen fibers and provides the most mechanical support when subjected to flexural tension; the spongiosa layer is made of highly hydrated glycosaminoglycans (GAGs) and serves as a lubrication layer for the fibrosa and atrialis layers; the atrialis layer contains collagen and radially aligned elastin fibers and sets out to provide support for reducing radial strains when the valve undergoes physiological loading [9,31,32].

While numerous studies have shown that the heart valve tissues exhibit anisotropic behaviors and found significant difference in mechanics and microstructure among the atrioventricular valve leaflets [33–35], obtaining collagen fiber orientation data and appropriate constitutive models to accurately reflect the anisotropic characteristic feature of each leaflet tissue is a challenging task. As such, we adopted an incompressible, isotropic, and hyperelastic constitutive model for the atrioventricular valve leaflet tissue, namely, the Lee-Sacks constitutive model [11] in the present work. The Lee-Sacks isotropic material model [11] provided a simple and computationally efficient formulation [36] and was used for approximating the biomechanical response of the leaflet tissue in the present work (the constitutive model verification results are provided in Appendix A). The second Piola–Kirchhoff stress, S, of the Lee-Sacks soft tissue model was formulated using an isotropic Fung-type material, wherein the contributions of the extracellular matrix and collagen fiber network were represented additively by neo-Hookean and exponential terms, respectively. The nonlinear stress–strain tissue response is captured by the following unconstrained constitutive model

$$\boldsymbol{S} = 2\frac{\delta \psi_{el}}{\delta \boldsymbol{C}} - K\ln(J)\boldsymbol{C}^{-1} \tag{1}$$

Here, ψ_{el} is an elastic strain energy function, C is the right Cauchy-Green deformation tensor, K is the bulk modulus, and J is the Jacobian of deformation. In the present work, incompressibility was enforced via a penalty method. In particular, K was set to 5000 kPa to satisfy near-incompressibility. The hyperelastic strain energy function was expressed as

$$\psi_{el} = \frac{c_0}{2}(I_1 - 3) + \frac{c_1}{2}\left\{\exp\left[c_2(I_1 - 3)^2\right]\right\} \tag{2}$$

where c_0, c_1, and c_2 are material coefficients, and $I_1 = trC$. Therefore, the term $\frac{\delta \psi_{el}}{\delta C}$ in Eq. (1) becomes

$$\frac{\delta \psi_{el}}{\delta C} = \frac{1}{2}\left(c_0 + 2c_1c_2(I_1 - 3)\exp\left[c_2(I_1 - 3)^2\right]\right)\mathbf{I} \tag{3}$$

2.3 Chordae Tendineae Modeling. The chordae tendineae play a critical role in ensuring proper heart valve closure; these branch-like collagenous tissues connect the leaflets to the papillary muscle heads to prevent leaflet prolapse into the left atrium during ventricular contraction. However, while individual chordae can be visualized via *ex-vivo* CT scan, individual chordae cannot be reliably visualized using clinically derived 3DE in humans [9]. Therefore, the geometric modeling of chordae tendineae from 3DE derived models relies on strategic simplifications to circumvent modeling limitations while accurately preserving their biological function. In the present work, we opted for a simplified, but robust, chordal topology approach introduced by Khalighi et al. [12]. Khalighi et al. demonstrated that a uniformly distributed, branchless chordal model with 15 ± 2 chords/cm^2 was able

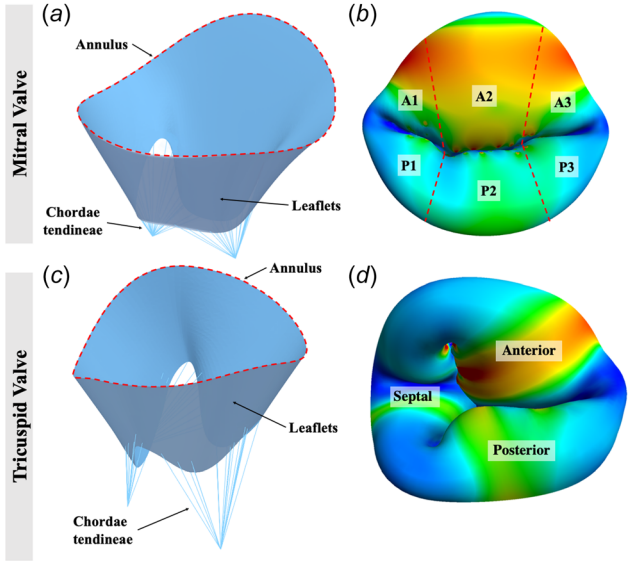

Fig. 3 Geometric representation of image-derived mitral and tricuspid valve FE models: (*a*) model of open mitral valve with annulus, leaflets, and chordae tendineae defined, (*b*) model of closed mitral valve with leaflet regions defined, (*c*) model of an open tricuspid valve with annulus, leaflets, and chordae tendineae defined, and (*d*) model of a closed tricuspid valve with leaflets defined. Mitral valve annular circumference was 12.3 cm and annular area projected onto the least squares annular plane was 11.0 cm^2. Tricuspid valve annular circumference was 13.1 cm and annular area projected onto the least squares annular plane was 12.0 cm^2.

to reproduce the ground truth results in predicting mitral valve closure to a high degree of accuracy. We uniformly distributed 17 chords/cm^2 over the chordae insertion zone of our valve models. The chords were modeled as tension-only 2-node linear springs that connect the leaflet insertion points to the papillary muscle tips. The mechanical behavior of the springs was considered mathematically within FEBio with a nonlinear force–displacement response where the tension was equal to zero up to a defined displacement value and the springs behaved linearly once the displacement threshold was reached.

The effective nonlinear spring force was defined as $F(x) = f_s \times G(x)$, where f_s is the user-defined spring force, $G()$ is a unit-less scaling function that defines the force–displacement behavior, and x is the change in spring length. The force–displacement scaling function was formulated as

$$G(x) = \begin{cases} 0, & x \le \delta \\ x - \delta, & x > \delta \end{cases} \tag{4}$$

where δ is the user-defined displacement-threshold. In the present work, we used $\delta = 5$ mm for both mitral and tricuspid valves. The chordal parameters were obtained through an iterative process in which we incrementally increased the spring tension force until equilibrium was achieved and the total tethering force on the papillary muscle tips agreed with those reported in the literature. While the spring constant variable was not explicitly used in the spring force formulation, one could derive the spring constant, k, by computing $k = \frac{dF}{dx}$. Given that $G(x)$ is a linear function, the spring constant was constant in all simulations.

2.4 Contact Potential. Atrioventricular valve leaflet contact can be particularly difficult to realistically model. In preliminary experiments using traditional contact models we frequently experienced unrealistic penetration of opposing leaflets, and failure of the solution to converge. Kamensky et al. recently described a potential-based contact formulation [13]. This contact formulation was implemented in FEBio after preliminary investigation and found it to be particularly well suited to allowing the valve leaflets to slide past one another, avoiding unrealistic penetration of opposed leaflets. The contact potential between the two objects of interest was approximated by the contact potential energy expressed as

$$E_c = \int_{\Omega_0^2}\int_{\Omega_0^1} \phi(r_{12}) d\mathbf{X}_1 d\mathbf{X}_2 \tag{5}$$

where $\mathbf{X}_1$ and $\mathbf{X}_2$ are in the reference configurations of the two contact bodies denoted by Ω_0^1 and Ω_0^2, respectively, $\phi(r_{12})$ is a contact potential kernel, and r_{12} denotes the Euclidean distance between two contact points.

The contact potential was described by the following force-separation law

$$-\phi'(r_{12}) = \begin{cases} \dfrac{k_c}{(r_{12})^{\alpha}} - c_2, & r_2 < r_{\text{in}} \\ c_1 (r_{12} - r_{\text{out}})^2, & r_{\text{in}} \le r_{12} < r_{\text{out}} \\ 0, & \text{otherwise} \end{cases} \tag{6}$$

where k_c is a dimensionless scaling factor for the contact force, r_{in} is the inner distance that governs the transition between parabolic and higher-order regions of the contact potential, r_{out} is the outer distance that defines the boundary of the contact surface, and α is the power of the contact potential. We refer interested readers to [13,18] for detailed information regarding the numerical implementation of the contact potential.

2.5 Solution Procedure. The valve medial surface was discretized into 4-node linear quadrilateral (Quad4) shell elements [37]. We applied fixed displacement boundary conditions to the outer circumference of the annulus edge and the papillary muscle tips. We deformed the model from diastolic to systolic configuration by prescribing a physiologically realistic systolic ventricular pressure orthogonal to the ventricular surface of the leaflets. Stress-free reference configuration (the initial segmented mid-diastolic geometry) was considered in the present work. Although the quasi-static response was sought, dynamic analyses were performed to achieve better simulation convergence. A mass damping scheme was employed with damping coefficient $C = 2000$ Ns/m to suppress the vibrational modes and to obtain the equilibrated solution. The implicit Newmark time integration scheme, along with an automatic time-stepping algorithm, was used to facilitate time advancement and maintain nonlinear solution convergence in the dynamic simulation. The material density considered for both mitral and tricuspid valves was 1 g/cm^3. The displacement and energy relative tolerances in FEBio were set to 0.001 and 0.01, respectively.

Figs. 3(*a*) and 3(*b*) provide a geometric visualization of the mitral valve model. The mitral model was discretized into 735 elements, 2965 elements, and 11689 elements for mesh convergence analysis. The material coefficients used for the mitral valve were: $c_0 = 200$ kPa, $c_1 = 2968.4$ kPa, and $c_2 = 0.2661$ [11]. We assumed 0.396 mm uniform thickness over the leaflets.

We applied 100 mm Hg ventricular pressure to the ventricular surface of the mitral valve. The pressure was first increased linearly over 0.005 s (consistent with Ref. [11]) to initiate the dynamic simulation. The pressure was then kept constant until the valve reached steady-state (full closure). The pressure evolution as a function of time was

$$p(t) = 100\,\text{mm Hg} \begin{cases} t/T, & t < T\,\text{s} \\ 1, & \text{otherwise} \end{cases} \tag{7}$$

where T is the ramp-up time scale and was set to 0.005 s. Once T is reached, the pressure load is maintained until steady-state. The

initial time-step increment was set to $\Delta t = 0.0001$ s. We terminated the simulation at 0.02 s. A total of 57 chords were attached to the mitral valve. The chordal force as a function of leaflet displacement was described by a nonlinear function in which zero tethering force was applied for the initial 5 mm displacement threshold to accurately reflect the chordal slack length. The chords were each prescribed an effectively spring force $F(x) = 30\,\text{mN}\,G(x)$ after the displacement threshold, where $G(x)$ is the scaling function defined in Eq. 4. The contact potential parameters for the fine mesh were: $k_c = 1$, $p = 4$, $R_{\text{in}} = 0.2$ mm, and $R_{\text{out}} = 0.5$ mm.

A visualization of the tricuspid valve model is shown in Figs. 3(*c*) and 3(*d*). The mesh densities for the coarse, medium, and fine meshes consisted of 761, 3044, and 12176 elements, respectively. The material coefficients used for the tricuspid valve were: $c_0 = 10$ kPa, $c_1 = 0.209$ kPa, and $c_2 = 9.046$ [38,13]. We assumed 0.396 mm uniform thickness over the leaflets. The peak systolic pressure value, 23.7 mm Hg [5,38], was applied to the tricuspid model

$$p(t) = 23.7\,\text{mm Hg}\begin{cases} t/0.01, & t < 0.01\,\text{s} \\ 1, & \text{otherwise} \end{cases} \tag{8}$$

We attached a total of 41 chords to the tricuspid valve; an chordal tension force, $F(x) = 20\,\text{mN}\,G(x)$, was applied to each chord. The contact potential parameters for the fine mesh were: $k_c = 1$, $p = 4$, $R_{\text{in}} = 0.25$ mm, and $R_{\text{out}} = 0.4$ mm.

All numerical simulations were performed on a high-performance computing system located at the Children's Hospital of Philadelphia, consisting of Intel Xeon CPU E5-2680 v3 computing nodes. Each node contains 24 cores, with 2.5 GHz core speed and 128 GB RAM per node. The CPU time of the mitral and tricuspid valve fine mesh models were 14 and 34 min, respectively.

2.6 Convergence Analysis. We examined the mean, 75th percentile, and 95th percentile of the 1st principal Cauchy stress and Green strain, together with the valve closure profiles of the three mesh models to assess the convergence. The mean values represent the average stress/strain over all elements. The 75th percentile and 95th percentile refer to the values that cover 75% and 95% of the stresses/strains, respectively. Mesh convergence was determined when the percentage of L^2 relative error norms was reduced to less than 5%. The L^2 relative error norms were defined as

$$L^2\,\text{relative error norm} = \sqrt{\frac{\sum_{i=0}^{N}(S_{\text{ref},i} - S_{\text{test},i})^2}{\sum_{i=0}^{N} S_{\text{ref},i}^2}} \times 100 \tag{9}$$

where $S_{\text{ref},i}$ represents the i^{th} index of the stress or strain time history with the fine mesh, $S_{\text{test},i}$ represents the i^{th} index of the stress or strain time history with either the coarse or medium mesh, and N represents the total number of time steps.

2.7 Uncertainty Analysis. Uncertainty analysis is an indispensable part of computational modeling. With numerous parameters involved in valve modeling, there is a need to better understand the role each parameter plays in affecting the final model responses. As such, rigorous sensitivity analyses were performed to identify the effect of the parameters and inform the robustness and predictive capability of the numerical models and approaches. Ultimately, such analyses correlate in vivo and in silico data such that reasonable tolerances and margins of error can be determined should such models be used in a translational setting.

We carried out two uncertainty analysis approaches (traditional and statistical) with the fine mesh mitral and tricuspid models. In the traditional approach, we explored the influence of the modeling parameters individually, while in the statistical approach, we utilized a polynomial chaos expansion (PCE) function to quantify the uncertainty in the FE model [39]. The parameters under consideration were the material coefficients in the Lee-Sacks constitutive models (coefficient c_0 in the neo-Hookean term, and coefficients c_1 and c_2 in the isotropic exponential term). We used the material coefficients reported in Lee et al. [11] and Kamensky et al. [13] to study the uncertainties in the mitral and tricuspid valve, respectively. Additionally, we explored the influence of the chordal displacement threshold and tension, as previous works suggested chordal rest length had significant impacts on valve closures [40–42]. We sampled five data points uniformly distributed within the range of ±50% of the baseline values used in the mesh convergence analyses.

Table 1 Uncertainty analysis parameters for the mitral and tricuspid valve

	Mitral		Tricuspid	
Input parameter	min.	max.	min.	max.
c_0	100.00	300.00	5.00	15.00
c_1	1484.20	4452.60	0.10	0.31
c_2	0.13	0.40	4.52	13.57
Chordal tension	15.00	45.00	10.00	30.00
Chordal length	2.50	7.50	2.50	7.50

For traditional sensitivity analysis, a total of five sample points uniformly distributed between the min. and max. values were used. For the statistical sensitivity analysis, a total of 45 randomly generated sample points were used. Note: only input parameters c_0, c_1, and c_2, were considered in the statistical sensitivity analysis.

We leveraged UncertainSCI for the statistical uncertainty analysis procedure, a Python-based toolkit that harnesses modern techniques to estimate the model and parametric uncertainty, with a particular emphasis on needs for biomedical simulations and applications [39]. This was achieved by interfacing UncertainSCI with the FEBio solver using via a Python subroutine within FEBio and FEBioUncertainSCI[5]. UncertainSCI used a polynomical chaos expansion function with a weighted approximate Fekete points (WAFP) method to randomly generate collocation points within the user-specified n-dimensional space (where the number of dimensions is determined by the number of input parameters) for sensitivity quantification. Unlike the traditional approach, where the parameters of interest were varied one at a time, UncertainSCI allowed for multiple variables such that the influence of input interactions may be examined. Furthermore, UncertainSCI provided quantitative measures of the uncertainties from the input parameters by computing the relative variance that each parameter contributed to the total variance, namely, the first-order Sobel index. This enables better evaluation and comparison of the model output uncertainty from the material constants. Uncertainty analysis was performed with the parameters listed in Table 1.

3 Results

We present verification and sensitivity analysis results of two image-derived valve models (mitral and tricuspid) to demonstrate the feasibility and robustness of the open-source software in the present work. The implemented contact potential algorithm substantially improved simulation instabilities associated with high-frequency oscillations and unphysical leaflet penetrations that occurred in valve dynamic simulations. For each valve model, we considered three mesh densities (coarse, medium, and fine). The length and width of each element were divided exactly in half within each level of refinement—resulting in a fourfold increase in mesh density as we refined the models. After we established the

[5] www.github.com/febiosoftware/FEBioUncertainSCI

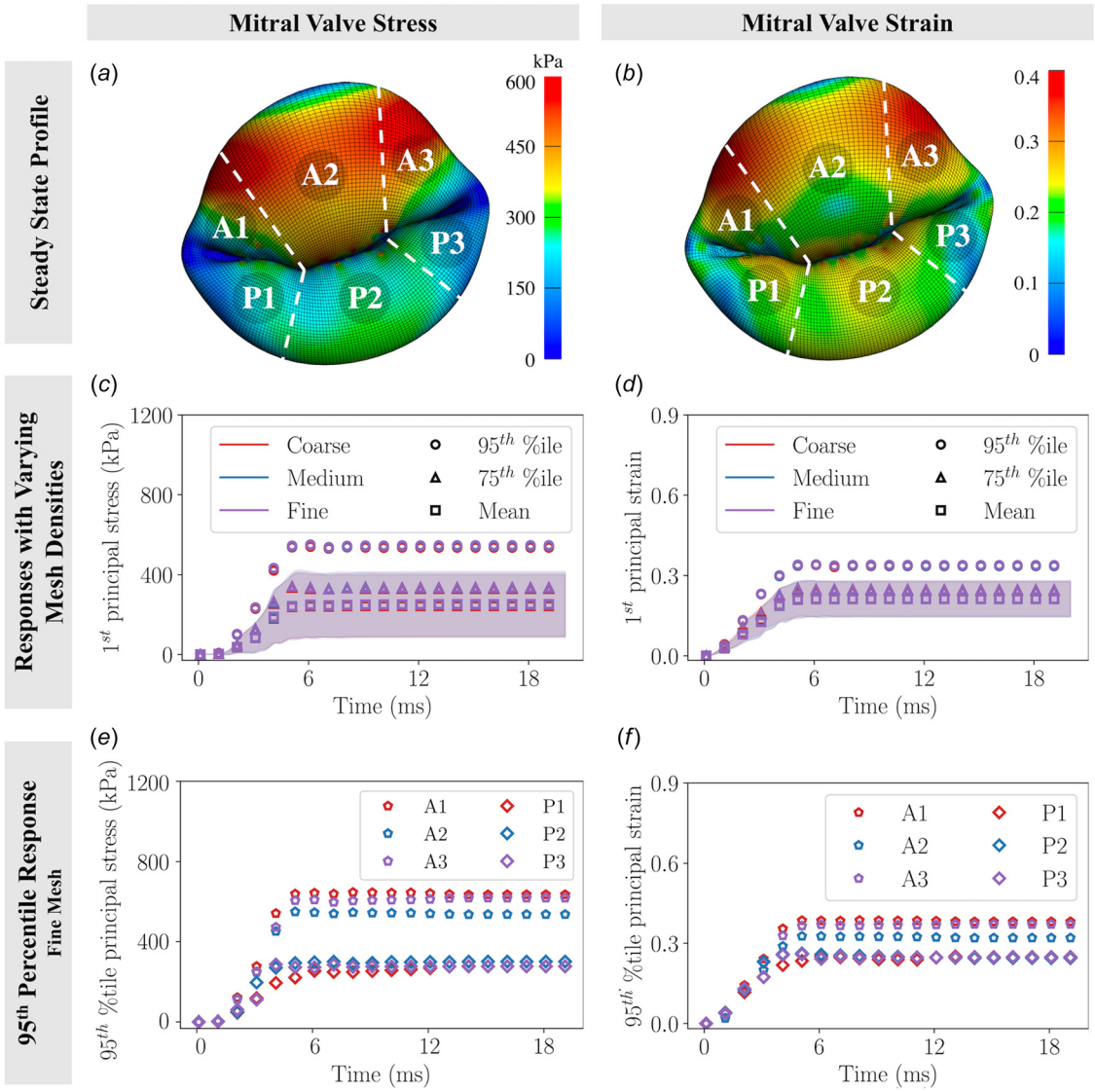

Fig. 4 Mitral valve stress and strain responses: (*a*) stress profile on the mitral valve at steady-state, (*b*) strain profile on the mitral valve at steady-state, (*c*) stress responses with coarse, medium, and fine meshes (shaded areas indicate standard deviations), (*d*) strain responses with coarse, medium, and fine meshes (shaded areas indicate standard deviations), (*e*) 95th percentile 1st principal stress responses on various mitral valve regions, and (*f*) 95th percentile 1st strain responses on various mitral valve regions. Results suggested that the anterior leaflet experiences higher stress and strain concentrations than the posterior leaflet.

convergence of the FE models, we used the fine mesh models to perform uncertainty quantification to study the effect of modeling input parameters on the biomechanical responses of atrioventricular valves.

3.1 Mitral Valve Verification. The means, standard deviations, 75th percentile, and 95th percentile of the stresses and strains of the whole mitral valve are shown in Figs. 4(*c*) and 4(*d*). We did not see substantial differences in stresses and strains related to mesh density. The sum of chordal tethering force on both papillary muscles was 6.84N.

Each mitral valve leaflet is anatomically divided into three scallop regions. Figs. 4(*e*) and 4(*f*) present the 95th percentile regional stresses and strains with the fine mesh. The results suggested that the anterior leaflet experiences a higher stress concentration (about two times higher than the posterior leaflet). The stress levels among the three scallop regions within each leaflet were similar. In our mitral model, the region A2 experienced lower strains compared to regions A1 and A3. However, region P2 presented similar strains in comparison to regions P1 and P3.

We evaluated a cross section of the mitral valve to assess valve closure of the three meshes (Fig. 5). The closing profiles were nearly identical among the three meshes, which suggested that the mesh densities used in the present work were sufficient to capture the valve closing behavior.

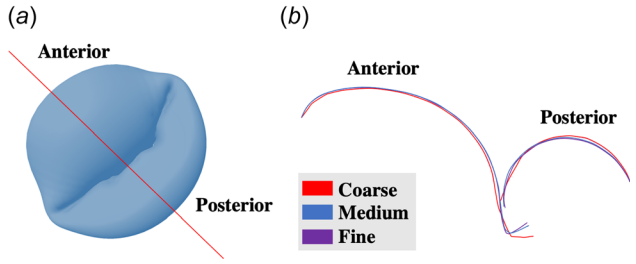

Fig. 5 Mitral valve closing profiles: (*a*) location at which the slices were made (red line), and (*b*) valve closure configurations for coarse, medium, and fine meshes at the anterior-posterior coaptation. Nearly identical closing profiles suggested that all of the tested mesh densities were sufficient to capture valve closing behavior.

Table 2 L^2 relative error norms (%) in various sections of the mitral valve

		1st principal stress			1st principal strain		
	Mesh refinement	mean	75th percentile	95th percentile	mean	75th percentile	95th percentile
Mitral	Coarse to medium	3.27	1.93	1.72	1.46	2.09	1.22
	Medium to fine	0.92	0.74	0.53	0.39	0.77	0.81
A1	Coarse to medium	3.76	2.19	2.61	5.36	1.79	0.83
	Medium to fine	0.99	0.90	0.73	1.66	0.61	0.50
A2	Coarse to medium	1.98	1.97	1.18	0.96	1.19	0.90
	Medium to fine	0.65	0.52	0.73	0.45	0.42	0.88
A3	Coarse to medium	2.07	1.16	2.10	1.02	1.05	1.04
	Medium to fine	1.16	1.09	0.70	1.17	0.73	0.63
P1	Coarse to medium	12.12	9.21	10.22	9.80	10.60	6.69
	Medium to fine	4.89	3.37	3.79	2.88	3.00	3.10
P2	Coarse to medium	10.17	8.14	7.16	5.44	5.88	7.15
	Medium to fine	2.10	2.05	2.41	0.92	1.36	1.70
P3	Coarse to medium	4.03	5.84	11.22	5.03	6.74	1.22
	Medium to fine	1.66	2.11	2.69	1.29	1.67	0.81

All L^2 relative error norms were under 5% in the medium to fine mesh refinement level, with the highest error norm (4.89%) in the mean 1st principal stress in region P1.

The convergence behavior was confirmed by the L^2 relative error norms, where we observed substantial error reduction with higher mesh density (Table 2). Region P1 reported the highest percentage error in mesh refinement level from medium to fine, with 4.89% relative error in mean principal stress. Nonetheless, this relative error was below the 5% threshold; indicating reasonable agreement between the medium and fine meshes. The mean, 75th percentile, and 95th percentile stresses of the whole mitral with the fine mesh at steady-state were 252.29 kPa, 336.45 kPa, and 546.22 kPa, respectively. The corresponding mean, 75th percentile, and 95th percentile strains at steady-state were 0.21, 0.25, and 0.34, respectively. Regional stresses and strains are reported in Appendix B, Table 4.

3.2 Tricuspid Valve Verification. The stress and strain responses of the tricuspid valve are shown in Fig. 6. Figs. 6(*e*) suggests that the anterior leaflet experienced the highest stress concentration, followed by the posterior leaflet, and finally the septal leaflet. On the other hand, the 95th percentile of strains was nearly identical among the leaflets (Fig. 6(*f*)). Similar to the mitral valve, we created three cross sections through the tricuspid valve to assess the closure configurations between leaflets (Fig. 7). Differences in valve closure profiles were observed with the models. The septal leaflet deformation with the coarse mesh showed significantly different characteristics in comparison to the two finer meshes. This suggested that the mesh density played an important role in capturing complex curvatures, as demonstrated in our specific image-derived tricuspid model. The sum of chordal tethering force on all papillary muscles was 2.38 N.

The L^2 relative error norms of the tricuspid model are presented in Table 3. The highest percentage error (in mesh refinement level from medium to fine) was found in the posterior leaflet, with 4.8% in the 95th percentile principal stress. All relative errors were below 5%. Therefore, the fine mesh of tricuspid model was a converged mesh. The mean, 75th percentile and 95th percentile stresses of the whole tricuspid valve at steady-state were 64.83 kPa, 82.62 kPa, and 127.27 kPa, respectively. The mean, 75th percentile, and 95th percentile strains at steady-state were 0.51, 0.59, and 0.63, respectively; stresses and strains on individual leaflet are reported in Appendix B, Table 5.

From Figs. 4(*e*)–4(*f*), we observed comparable differences in stresses and strains among the mitral leaflet regions. However, Figs. 6(*e*)–6(*f*) demonstrated that small changes in leaflet strains lead to substantial differences in the corresponding stresses among the tricuspid leaflets. To elucidate this disparity, we performed an uni-axial test on a single element square specimen for both the mitral and tricuspid material parameters. A total of 200 mN nodal force was applied to the top and bottom edge of the specimen, respectively. The stress–strain curves for the mitral and tricuspid valve are shown in Fig. 8. As shown in Fig. 8, given that the tissue properties for the mitral valve leaflet were stiffer, the stress–strain curve exhibited a quadratic relationship. On the other hand, the tricuspid valve material properties exhibited a slightly more flexible behavior, resulting in an exponential stress–strain relationship. That said, the stress–strain curve for the tricuspid valve tissue has a greater rate of change in slope. As such, the leaflet strains were relatively insensitive to the corresponding stresses as observed in Figs. 6(*e*)–6(*f*).

3.3 Traditional Sensitivity Analysis. The 95th percentile of the 1st principal stresses and strains at steady-state are presented in Fig. 9. The mitral and tricuspid valve modeling parameters demonstrated different influences on the stress and strain responses in the valve leaflets. Among the material coefficients for the mitral valve, the material coefficients in the isotropic exponential term (c_1 and c_2) had the most significant effect on both stresses and strains—with approximately the same minimum, maximum, and interquartile range (Figs. 9(*a*) and 9(*b*)); material coefficient c_0 had an inconsequential influence on the stresses but had a strong influence on the strain response. Additionally, Figs. 9(*a*) and 9(*b*) show that the chordal displacement threshold and tension force had opposite effects in stresses and strains. We observed that a higher chordal displacement threshold lead to higher stresses and strains; contrarily, increasing chordal tension forces yielded reduced mitral valve mechanical responses. An opposite behavior regarding the effect of the chordal displacement threshold and tension force was seen in the tricuspid valve stress responses (Fig. 9(*c*)). Specifically, greater chordal tension and lower chordal displacement threshold correspond to higher leaflet stress. Further, Fig. 9(*d*) indicates the chordal displacement threshold and tension force had insignificant effects on tricuspid strains. In terms of material coefficients, Figs. 9(*c*) and 9(*d*) suggest that the tricuspid model was most sensitive to the coefficient c_2 (in agreement with the mitral model). In contrast, coefficients c_0 and c_1 had negligible effects.

Figure 10 suggests the opposing behavior for the mitral and tricuspid valve in relation to chordal displacement threshold and tension is associated with the valve geometry between the mitral and tricuspid valve. For the mitral valve, a higher displacement threshold and lower chordal tension led to more tenting on the anterior

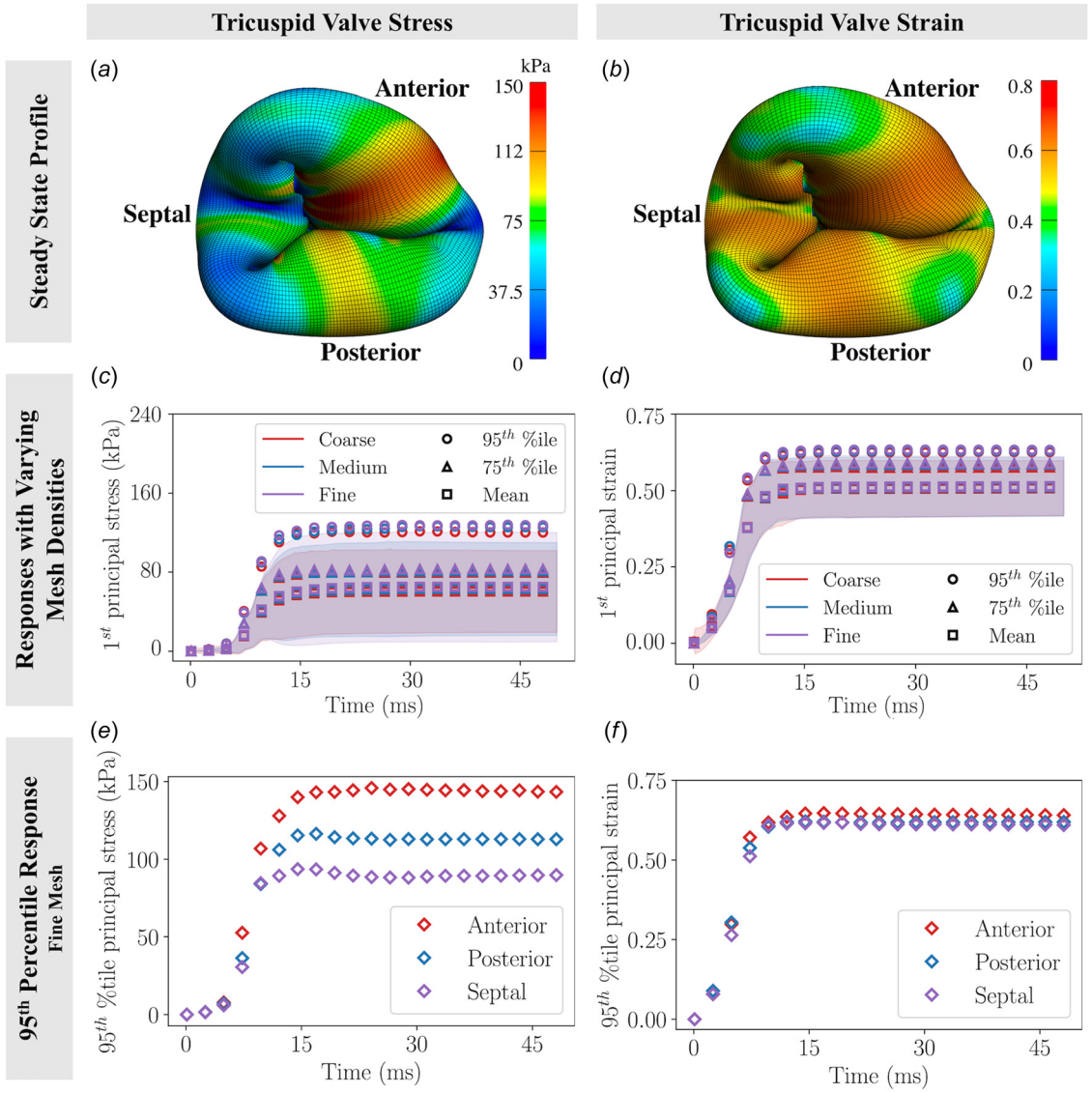

Fig. 6 Tricuspid valve stress and strain responses: (*a*) stress profile on the tricuspid valve at steady-state, (*b*) strain profile on the tricuspid valve at steady-state, (*c*) stress responses with coarse, medium, and fine meshes (shaded areas indicate standard deviations), (*d*) strain responses with coarse, medium, and fine meshes (shaded areas indicate standard deviations), (*e*) 95th percentile 1st principal stress responses on various tricuspid valve leaflets, (*f*) 95th percentile 1st principal strain responses on various tricuspid valve regions. While results suggested that the anterior leaflet experienced higher stress concentrations than the posterior and septal leaflets, 95th percentile 1st principal strains were nearly identical among the leaflets.

Table 3: L^2 relative error norms (%) in various sections of the tricuspid valve

		1st principal stress			1st principal strain		
	Mesh refinement	mean	75th percentile	95th percentile	mean	75th percentile	95th percentile
Tricuspid	Coarse to medium	6.94	3.80	5.18	1.38	2.22	1.65
	Medium to fine	3.33	2.63	2.05	0.59	0.86	1.62
Anterior	Coarse to medium	5.25	1.17	2.46	1.39	0.78	2.04
	Medium to fine	4.28	1.49	4.02	0.80	0.88	1.85
Posterior	Coarse to medium	5.58	4.80	9.56	1.10	2.59	3.77
	Medium to fine	3.27	3.12	4.80	0.56	1.09	1.52
Septal	Coarse to medium	10.78	5.73	3.57	3.33	3.59	2.92
	Medium to fine	2.25	2.41	1.78	0.64	1.04	0.76

All L^2 relative error norms were under 5% in the medium to fine mesh refinement level, with the highest error norm (4.8%) in the 95th percentile of the 1st principal stress in the posterior leaflet.

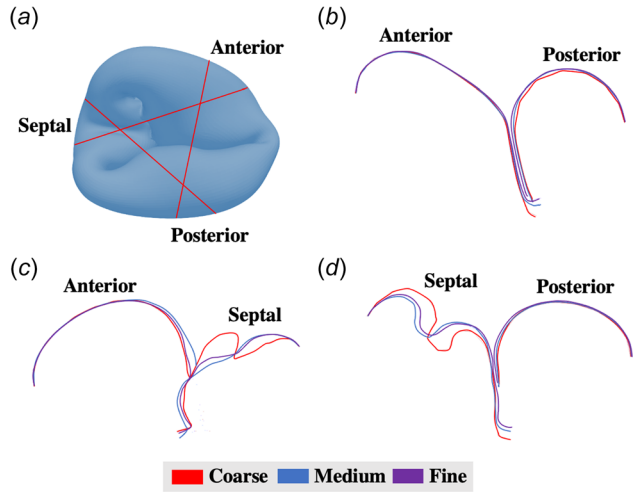

Fig. 7 Tricuspid valve closing profiles: (*a*) locations at which the slices were made (red lines); valve closure configurations for coarse, medium, and fine meshes at the (*b*) anterior-posterior coaptation, (*c*) anterior-septal coaptation, and (*d*) posterior-septal coaptation. Septal leaflet deformation with the coarse mesh showed significantly different characteristics in comparison to the two finer meshes, suggesting that the mesh density played an important role in capturing complex curvatures, as demonstrated in the tricuspid model.

leaflet, and therefore, resulted in higher bending stress on the A2 region. To that end, a noticeable increase in stress was observed on the A2 region of the mitral valve. On the contrary, for the tricuspid valve, a higher displacement threshold and lower chordal tension provided more flexibility for the septal leaflet to "flatten" out as opposed to the "buckled" configuration. This essentially reduced the bending on the leaflets. Therefore, the tricuspid valve exhibited lower stress with a higher displacement threshold and lower chordal tension.

The systolic configurations of the mitral and tricuspid valves at steady-state are presented in Figs. 11 and 12 to assess the influence of chordae modeling parameters on valve closure. Models with higher displacement threshold or lower chordal tension force displayed noticeable billowing, or leaflet prolapse into the atrium. Alternatively, models with early or excessive tensioning of the chordae demonstrated poor coaptation, indicating inadequate valve closure, and potential regurgitation.

3.4 Statistical Sensitivity Analysis. To facilitate the statistical sensitivity analysis, we applied a fourth polynomial order PCE

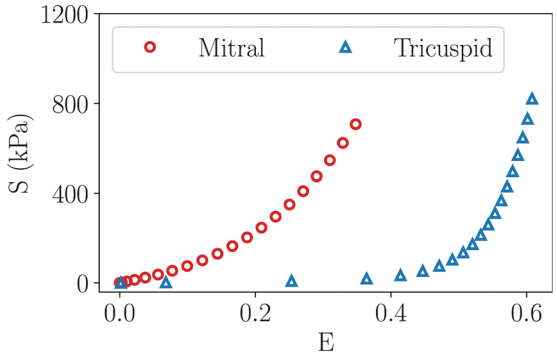

Fig. 8 The uni-axial stress–strain response comparison between the mitral and tricuspid properties. The mitral tissue displays a quadratic stress–strain relationship, whereas the tricuspid tissue displays an exponential relationship.

function to identify the sampling points in the material parameter space for FE analyses. We first assessed the sensitivity indices from interactions between parameters (i.e., the output uncertainty due to variations from two or more parameters). The relative variances obtained were small—less than 0.005—indicating that the material parameters contribute independently to the uncertainty of the model output.

The total sensitivities of the material constants were reported in Fig. 13. The statistical results suggested material coefficient c_1 was the most dominant, with Sobel index 0.71 for stresses and 0.47 for strains for the mitral valve. Similar to the findings in the traditional approach, material constant c_0 had negligible effects on mitral valve stresses (Fig. 13(*a*)), but it was the second-highest contributor to the total output variance on mitral valve strains (Fig. 13(*b*)). In the tricuspid model, material coefficient c_2 contributed the most to the model uncertainty—c_2 had a Sobel index of 0.91 and 0.95 in stresses and strains, respectively. In contrast, the Sobel indices for material coefficients c_0 and c_1 were well below 0.1 (Figs. 13(*c*) and 13(*d*)).

4 Discussion

Our long term goal is to develop a robust, open-source computational framework for the modeling of atrioventricular valves from 3D images to inform valve repair in children with congenital heart disease. We have taken the first step to achieve this by integrating and extending established open-source tools for cardiac image processing and finite element analysis [24–29,39]. This work forms an initial foundation for the collaborative development and application of biomechanical modeling to investigate the effect of image-derived, patient-specific valve structure on leaflet stress and strain. This, in turn, may inform the design and application of more durable valve repairs [43]. While our driving application is congenital heart disease, the tools described are fundamentally applicable to any population.

In seminal work on the mitral valve, Votta et al. observed that the stresses on the leaflet belly were in the range of 130 to 540 kPa on the anterior leaflet and 60 to 279 kPa on the posterior leaflet [44] at the systolic pressure of 120 mm Hg; Wang et al. reported a maximum principal stress of 160 kPa on the anterior leaflet midsection at 110 mm Hg peak systolic pressure [45]; Lee et al. found the maximum radial and circumferential stresses on anterior belly to be 509.5 ± 38.4 kPa and 301.4 ± 12.2 kPa at 90 mm Hg peak transvalvular pressure [11]. In our study, the 95th percentile principal stresses on the anterior and posterior belly at 100 mm Hg peak pressure was 536.16 kPa and 300.47 kPa, respectively. Our results agreed well with those reported in the literature; the differences in the stress values can be explained by differences in image-derived model structure and modeling approaches, including different material constitutive models, transvalvular pressure, and chordal tension force. As demonstrated in the sensitivity analysis, variations in chordal tension force and displacement threshold can lead to more than 50 kPa difference in principal stresses. In addition, our analyses suggested that overall, the anterior leaflet had higher principal stresses than the posterior leaflet, consistent with prior studies. In terms of strains, Rausche et al. determined that the maximum principal strains were 0.13 ± 0.047 on the ovine anterior mitral valve leaflet [46]. El-Tallawi et al. quantitated the strain of 32 normal mitral valves from 3DE images and found the average strains on the anterior and posterior leaflets were approximately 0.08 and 0.09, respectively [47]. The strain values obtained in our study were slightly higher than those reported from in vivo and image quantitation studies. We found the average Green strains on the A2 and P2 regions were 0.27 and 0.23, respectively.

Of the previous studies on the FE modeling of tricuspid valves, Stevanella et al. reported higher maximum principal anterior leaflet stress (430 kPa) than posterior leaflet (120 kPa) at 23.7 mm Hg [38]; Kong et al. reported average principal stress of 37–80 kPa,

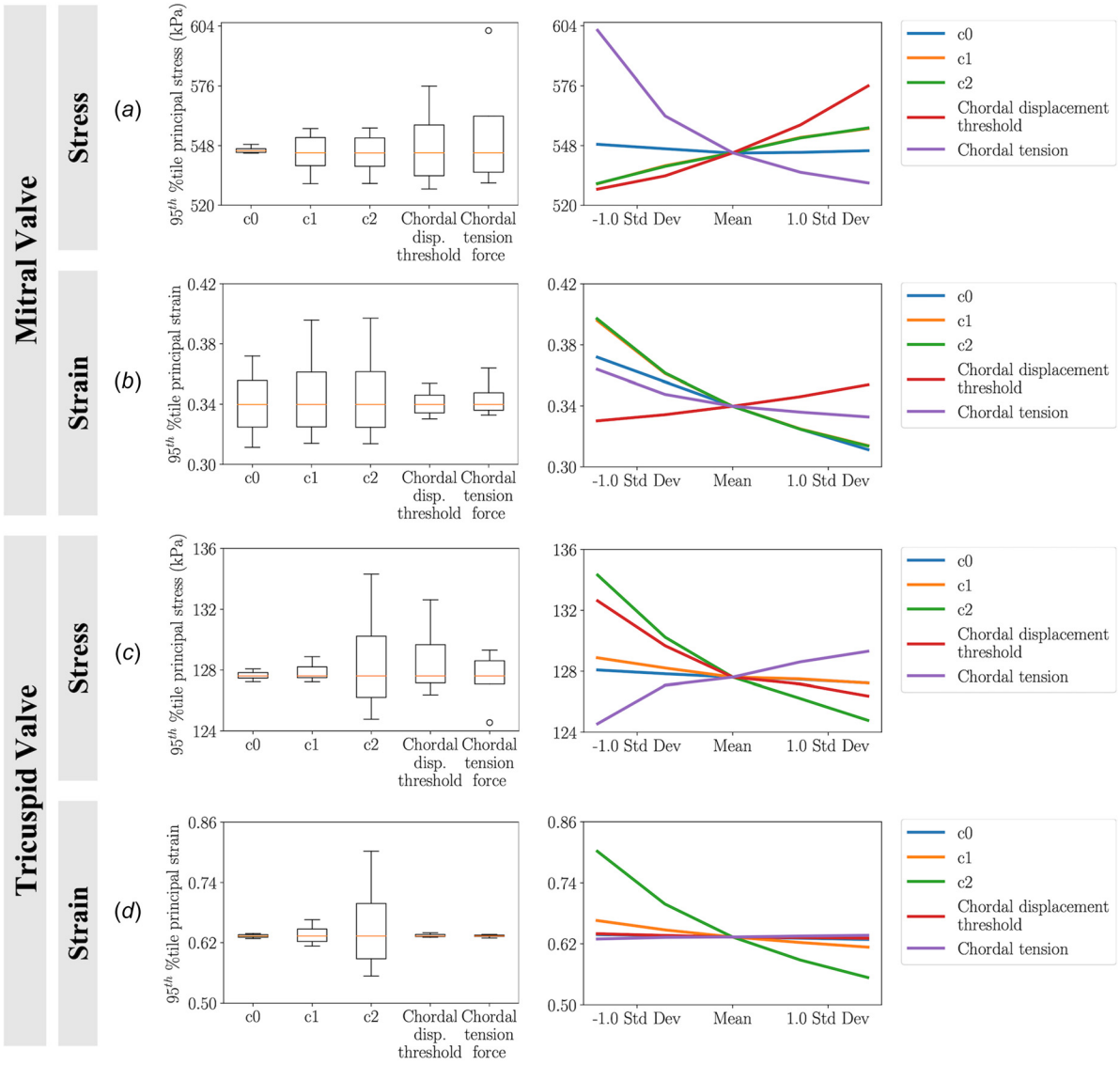

Fig. 9 The resulting sensitivity in the 95th percentile 1st principal stresses and strains from various modeling parameters: (a) sensitivity of stress in the mitral valve, (*b*) sensitivity of strain in the mitral valve, (*c*) sensitivity of stress in the tricuspid valve, and (*d*) sensitivity of strain in the tricuspid valve. The main box-plots demonstrate the spread of skewness of the stresses and strains for each individual modeling parameter. The line plots display the relations between the modeling parameters and the stresses/strains. Results suggested that the mitral valve stresses and strains were most sensitive to material coefficients c_1 and c_2, with c_0 displaying additional influence on strains; tricuspid valve stresses and strains were most sensitive to material coefficient c_2. For the mitral valve, increased chordal displacement threshold led to higher stress/strain and increased chordal tension led to lower stress/strain, whereas the tricuspid valve displayed the opposite responses for stress and negligible responses for strain. Note: In (*a*) and (*b*), the curve for c_1 is beneath the curve for c_2.

25–91 kPa, 24–63 kPa on the anterior, posterior, and septal leaflets, respectively, at midsystole under the same peak transvalvular pressure [5]; Laurence et al. reported the von Mises stress of 24.7 ± 7.9 kPa (anterior), 30.6 ± 10.9 kPa (posterior), and 41.9 ± 8.6 kPa (septal) on the tricuspid leaflet belly at 25 mm Hg peak pressure [48]. Our tricuspid stress values agreed well with Kong et al.'s approximations. The discrepancies between our results and Stevanella et al. may be due to differences the geometry of the model. The same constitutive model and material coefficients were used in Laurence et al. [48]. However, Laurence et al. reported slightly lower stresses. The relatively smaller valve geometry can be attributed to the smaller valve geometry in their work. In addition to the stresses, Stevanella et al. reported circumferential and radial strains of 0.13–0.16 and 0.25–0.30 on the anterior leaflet belly [38]; Kong et al. reported average principal strains of 0.19–0.26, 0.07–0.17, and 0.11–0.21 on the anterior, posterior, and septal leaflets, respectively [5]; and Laurence et al. reported maximum principal strains of 0.33 ± 0.07 (anterior), 0.41 ± 0.06 (posterior), and 0.44 ± 0.03 (septal) on the tricuspid leaflet belly. Our strain predictions were slightly higher than the reported values. We further compared our strain predictions to in vivo studies, Marthur et al. found that the maximum strains reported on the anterior, posterior, and septal leaflet bellies were 0.82, 0.32, and 0.41, respectively [49]. In comparison, the 95th percentile strain on the anterior, posterior, and septal leaflets from our FE analyses were 0.64, 0.62, and 0.61, respectively. Given that our sensitivity analysis suggested the chordal displacement threshold and tension force were inconsequential to tricuspid valve strains, the differences observed could be due to a combination of differences in constitutive models and valve geometry.

The valve geometries in the present work were derived from images but simplified to create representative models for this

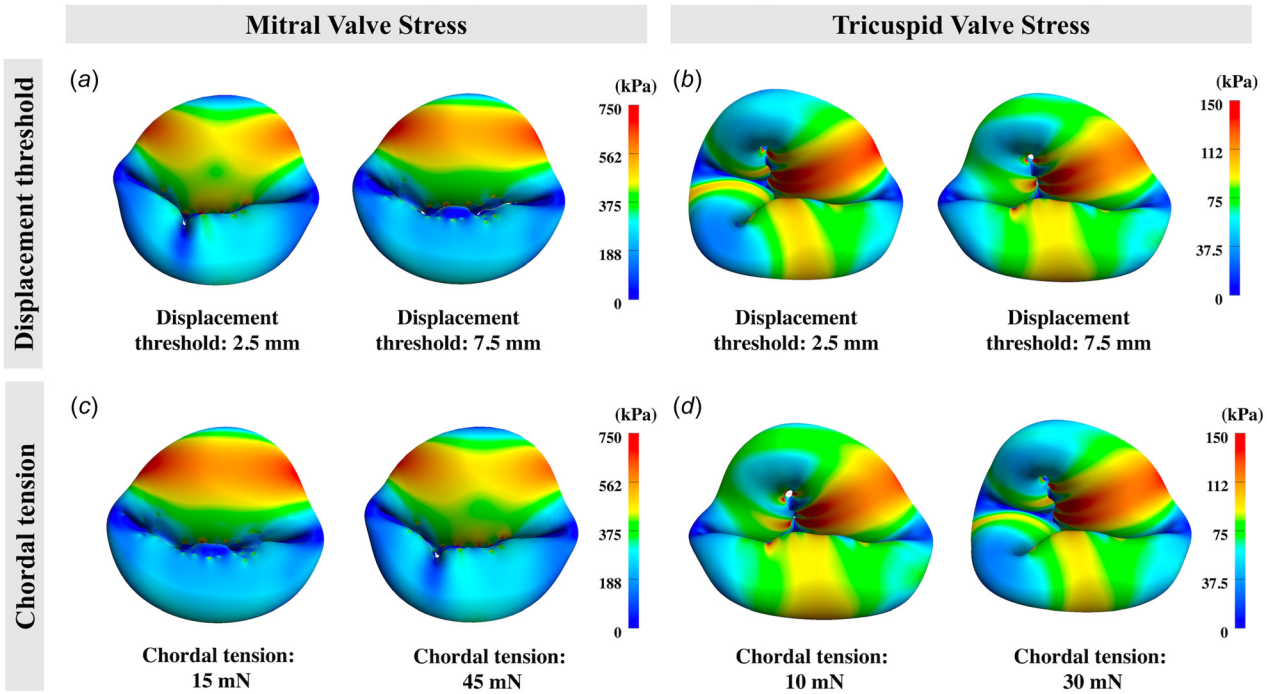

Fig. 10 The 1st principal stress profiles at steady-state on the mitral and tricuspid valves: (*a*) and (*b*) demonstrate the differences in the stress profiles due to varying chordal displacement threshold (i.e., chordal slack length). (*c*) and (*d*) demonstrate the differences in the stress profiles due to varying chordal tension. Higher displacement threshold and lower chordal tension led to high stress on the mitral valve, but lower stress on the tricuspid valve.

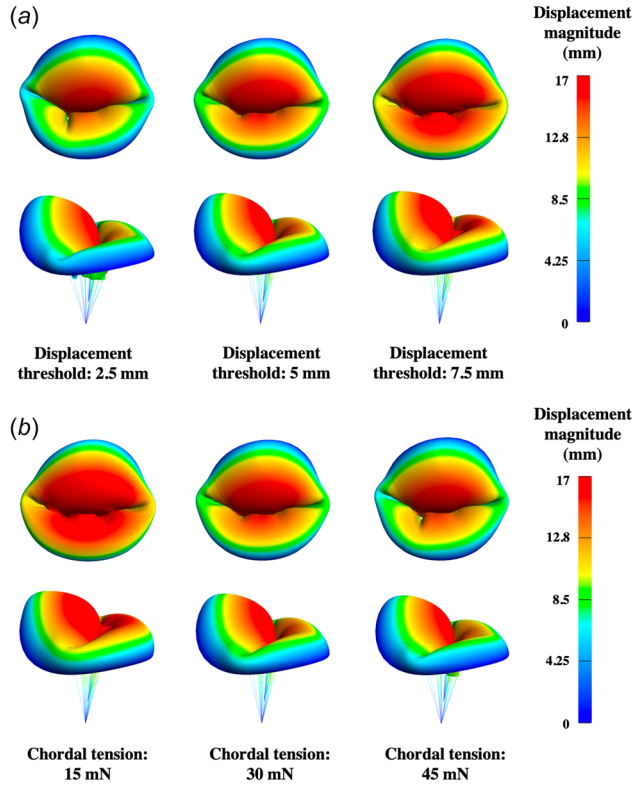

Fig. 11 Mitral valve systolic configurations resulting from variations in chordae modeling parameters: (*a*) systolic configurations subject to various displacement threshold with a fixed chordal tension at 30 mN and (*b*) systolic configurations subject to various chordal tension with a fixed displacement threshold at 5 mm. Higher displacement threshold or lower chordal tension force led to models with noticeable billowing.

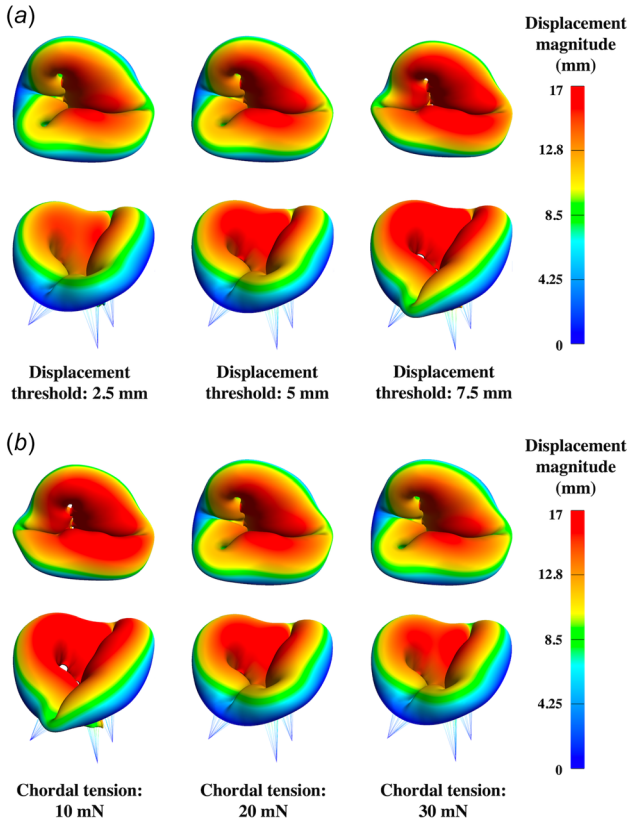

Fig. 12 Tricuspid valve systolic configurations resulting from variations in chordae modeling parameters: (*a*) systolic configurations subject to various displacement threshold with a fixed chordal tension at 20 mN and (*b*) systolic configurations subject to various chordal tension with a fixed displacement threshold at 5 mm. Higher displacement threshold or lower chordal tension force led to models with noticeable billowing.

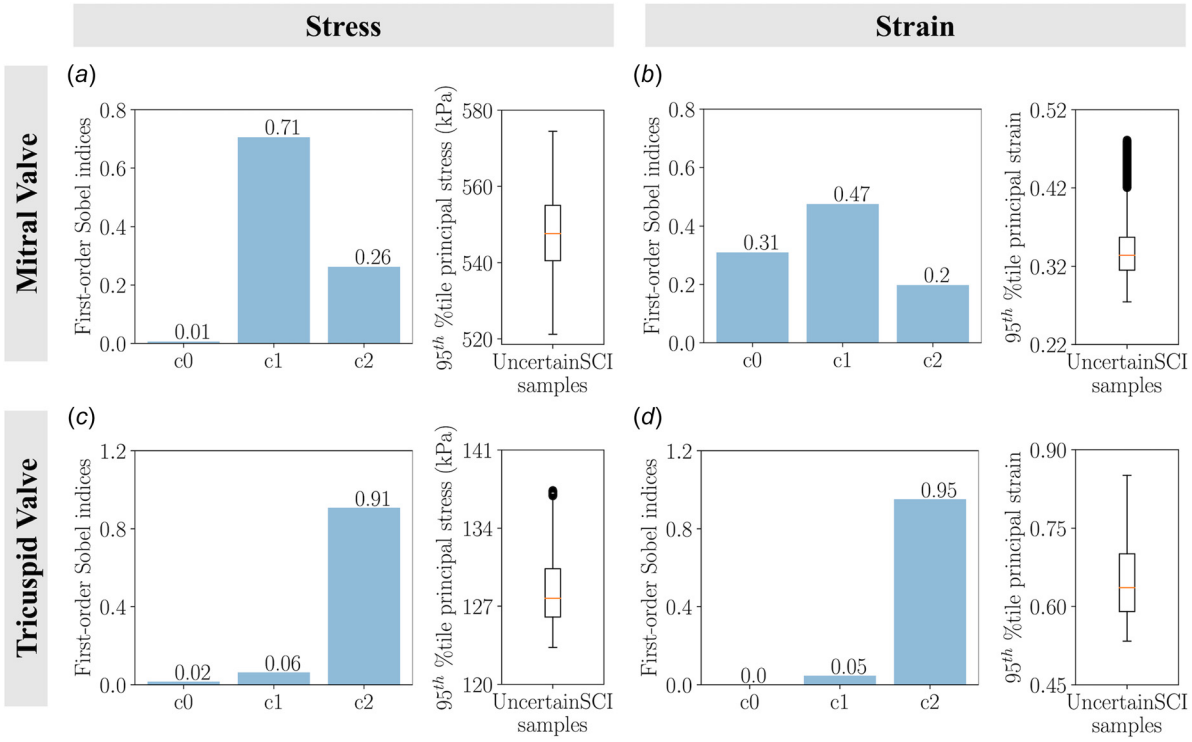

Fig. 13 The main sensitivity of the stresses and strains as a function of material constants using UncertainSCI: (*a*) Uncertainty in mitral valve stress, (*b*) uncertainty in mitral valve strain, (*c*) uncertainty in tricuspid valve stress, and (*d*) uncertainty in tricuspid valve strain. Bar plots denote the first-order Sobel indices and box plots depict the spread of stresses and strains of 45 UncertainSCI samples with fixed polynomial chaos expansion order 4 and fixed random number generator seed 0. Results were consistent with the traditional approach, with c_1 and c_2 influencing mitral valve stresses and strains (with additional influence of c_0 on strains), and c_2 influencing tricuspid valve stresses and strains.

initial investigation. However, anatomically accurate valve geometries are critical in determining the stress profiles on the mitral leaflets [9,12,48]. For example, Jimenez et al. suggested that the annular geometry had a direct consequence to the chordal force distribution [50]. Sacks et al. [9] observed that the segment A2 had the highest stresses on some models. While we also observed high-stress concentration on segment A2, in our specific mitral model segments A1 and A3 had slightly higher stresses—possibly due to variations in the annular and leaflet geometry in our specific model. Notably, the stress distribution of our mitral valve FE model agreed well with the model in a previous study with similar mitral annular shape [51]. This highlights the importance of image-derived patient-specific FE models in order to generate insights relevant to that specific valve geometry.

Computational modeling of atrioventricular valve dynamics has historically been a challenge due to numerical instability that arises from leaflet contact. Frequently, researchers had to sacrifice solution accuracy (as obtaining a converged solution was difficult) by terminating simulations based on a fixed number of iterations within each time-step rather than by a set residual [52,53]. Although highly refined commercial packages such as LS-DYNA[6] and ABAQUS[7] made obtaining converged solutions possible, any such simulations required a time-step of 10^{-6} s or less [13,18]. Further, high-resolution simulations can take anywhere from 88 min [15] to more than 20 days to run with explicit time integration scheme [54]. Kamensky's volume potential approach [13] introduced a novel modeling method in contact mechanics, providing a robust and computationally efficient strategy to overcome the challenges encountered in atrioventricular valve FE modeling. We have now implemented this powerful methodology in FEBio. Together with the implicit time integration scheme available in FEBio, our models were able to achieve satisfactory systolic configurations in well under an hour using a single CPU with 24 cores.

Computational models of atrioventricular valves have become increasingly accurate at representing physical reality. However, these simulations often do not capture the impact of parameter uncertainty in their predictions [55]. As such, we performed uncertainty analysis using both traditional and statistical approaches to determine the most significant tissue material constants and chordal configuration on the biomechanical response of our mitral and tricuspid valve FE models. Our results indicated that the material constants in the Lee-Sacks model, as well as the chordal displacement threshold and tension, may have varying degrees of influence in image-derived models of the tricuspid and mitral valve. This highlights 1) the need for population-specific, and possibly patient-specific tissue constitutive models for atrioventricular valves, and 2) the importance of anatomically accurate chordal length and properties for the most accurate assessment of the leaflet stress and strain.

Consistent with our analysis, prior work has demonstrated that valve dynamics are highly influenced by chordal length and displacement threshold [41,42]. As such, substantial effort has been dedicated to accurately reconstructing the geometry and topology of chordae tendineae using high-resolution micro-CT imaging of static excised animal hearts [9,16,45]. Notably, micro-CT cannot currently be applied to living humans or beating hearts. Further, it is not currently feasible to visualize individual chordae in living humans using readily available 4D imaging techniques such as 3DE. As such, several approaches have been used to approximate chordal length and geometry in the absence of detailed knowledge of chordal structure. Mansi et al. approximated the chordal length using the distance between papillary muscle tips and leaflet free edge in end-diastole [41]. Kong et al. first assumed the chordae

[6]http://www.lstc.com/products/ls-dyna
[7]https://www.3ds.com/products-services/simulia/products/abaqus

were straight and branch-less, then iteratively adjusted the chordal length until the FE leaflet model matched CT images of the leaflets in systole. [5]. Khalighi et al. developed a simplified, but functionally equivalent, framework for modeling the chordae tendineae when they cannot be visualized in the 3D image [8]. Specifically, Khalighi et al. proposed to approximate the mitral chordae tendineae topology and geometry as branch-less chords uniformly distributed on the leaflets. The chordal lengths were estimated as the distance from the papillary muscle tips to the leaflet insertion points at systolic configuration. While this method provided accurate leaflet stress and strain response for mitral valve, validation in application to the tricuspid valve has yet be demonstrated. In some tricuspid valve studies, chords are applied only to leaflet edge [17,18]. However, in our experience distributing chordae only on the free edge resulted in significant billowing of the valve leaflets. In our work on both valves, we adopted a combination of these techniques to model the topology of the chordae tendinae, similar to the approach as Khalighi et al., but applied a fixed density of chords to an anatomic area of chordal insertion extending inward from the leaflet edge. In the future, it will be essential to conduct validation studies examining the influence of chordal density and chordal insertion zone area on the stress, strain, and profile of atrioventricular valves under load.

The applied chordal tension force in our study was obtained through an iterative process until the total tethering force on the papillary muscle tips agreed with those reported in the literature and created realistic valve closure in comparison to the images from which they were derived. The total tethering forces in our mitral valve and tricuspid valve FE models were 6.84 N and 2.38 N, respectively. These values fall within the range of total tethering forces in the literature, which were 4 to 13.5 N for the mitral valve [9,38,44,56], and 2.02 to 4.95 N for the tricuspid valve [5].

Finally, we demonstrated the integration of a recently developed statistical uncertainty analysis toolbox, UncertainSCI, into FEBio. Our UnscertainSCI-based statistical analysis agreed well with the findings from traditional analysis, which demonstrated the fidelity of the WAFP-based PCE method for uncertainty quantification. This WAFP-based PCE function was able to efficiently quantify the sensitivity of model input parameters to model response with significantly fewer sample points than standard Monte Carlo methods [39]. In addition, this approach offered further insights into the exact uncertainty measures from each input parameter, which were not quantifiable using the traditional approach. This provided additional information regarding the sensitivity that each parameter induced in the model. We computed the main sensitivity analysis with various PCE orders and random number generators (Appendix C). We did not observe significant differences in the sensitivity indices among the PCE orders and random number generators. This indicates the reliability of the WAFP-based PCE method for predicting sensitivities in our present work and in future applications.

5 Limitations and Future Work

Valve geometry greatly contributes to the biomechanical function of the valve. In the future, we hope to perform more clinically relevant studies, including comparison of dysfunctional valves to normal valves. Important parameters relevant to valve leak (regurgitation), such as leaflet coaptation and coaptation gaps, will be assessed [18]. Further, variation and alteration of valve structure can be used to understand the effect of valve geometry on valve stress and strain which may be relevant to valve repair durability [9,43]. In this setting, "surgical" alteration of such valves, emulating existing and novel repair techniques, could be used to optimize and inform surgical repairs before they are attempted in humans [18,57].

To the authors' knowledge, there is currently no open-source, ready-to-use mesh generation package for lofting valve surfaces from contour curves or the generation of shell mesh from an image-derived model. While the main components of model creation are open-source, we utilized a commercial CAD program to loft and mesh the leaflets using image-derived segmented models as a template. In the future, we hope to expand the capability to create and alter valve shell models directly within SlicerHeart and FEBio [18,57].

In this study, we utilized existing constitutive models derived from adult mitral and tricuspid valves. While this allows realistic comparison to existing work, and a means for comparison of the valve biomechanics with variation of a baseline structure, it is likely that the adult-derived constitutive models do not accurately describe the mechanical properties of the wide range of ages and valve types present in congenital heart disease. This emphasizes that despite the tremendous progress in atrioventricular valve modeling over the past decade [8,9,14,15,18,48], patient-specific clinical translation of in silico valve studies remains a challenge due to the potential variability of constitutive models and tissue parameters for valve leaflets.

Given the obstacles in obtaining human tissue for biaxial mechanical testing, to date, most atrioventricular valve FE analyses have adopted existing material properties obtained from animal or cadaveric tissue models [11,38]. However, human tissue properties may be significantly different from animals [5,58,59], and there are not animal model equivalents for every type of valve morphology or stage of development. This challenge is further accentuated in pediatrics and congenital heart disease. Specifically, it is unlikely existing constitutive models accurately describe the mechanical properties of the wide range of ages and valve types present in this complex population. Further work is needed to develop a framework for the development of age and pathology-specific constitutive models for this diverse population, as well as refinement of applicable leaflet shape fitting approaches to mitigate this impediment to translational application when precise constitutive models are not available [43].

Finally, the present work reported on the investigation of the biomechanical response at atrioventricular valve closure while varying leaflet properties and chordal parameters. However, in the future the application of fluid structure interactions (FSI) will allow for the application of more realistic loading conditions, as well as a more direct means of assessing valve regurgitation.

6 Conclusion

We describe the preliminary implementation of an image-to-FE modeling workflow for the biomechanical modeling of atrioventricular valves. While the driving application underlying the development of this evolving open-source framework was to inform a more disciplined and rigorous approach to the assessment of valve failure in children with congenital heart disease, it is fundamentally applicable to a wide range of valve science. Our initial stress and strain results yielded excellent agreement compared with the literature and we provided a detailed sensitivity analysis of the FE modeling parameters using both traditional and statistical methods. Future work will focus on optimization, validation, and application to investigate the biomechanics of dysfunctional atrioventricular valves.

Acknowledgment

This work was supported by NIH R01HL153166, R01GM083925, U24EB029007, Big Hearts to Little Hearts, a Children's Hospital of Philadelphia (CHOP) Frontier Fund (Pediatric Valve Center), The Cora Topolewski Fund at CHOP Pediatric Valve Center, and the Canarie Research Software foundation.

Funding Data

- NIH (Grant Nos. R01HL153166, R01GM083925, and U24EB029007; Funder ID: 10.13039/100000002).

Appendix A: Constitutive Model Implementation Verification Results

Here, we provide verification results of an equibiaxial test proposed by Sun et al. [60]. The geometry of the equibiaxial test, shown in Fig. 14(*a*), consists of a 25 mm × 25 mm square specimen that was discretized into 400 quadrilateral (Quad4) elements. A total of 10 N nodal force were applied to the top, bottom, left, and right edge of the specimen, respectively. The material properties of specimen were: $c_0 = 67.6080$ kPa, $c_1 = 13.2848$ kPa, $c_2 = 38.1878$ and $K = 25000$ kPa [36]. The stress- strain curve approximation produced by FEBio demonstrated excellent alignment compared with the IGA approximation reported by [36].

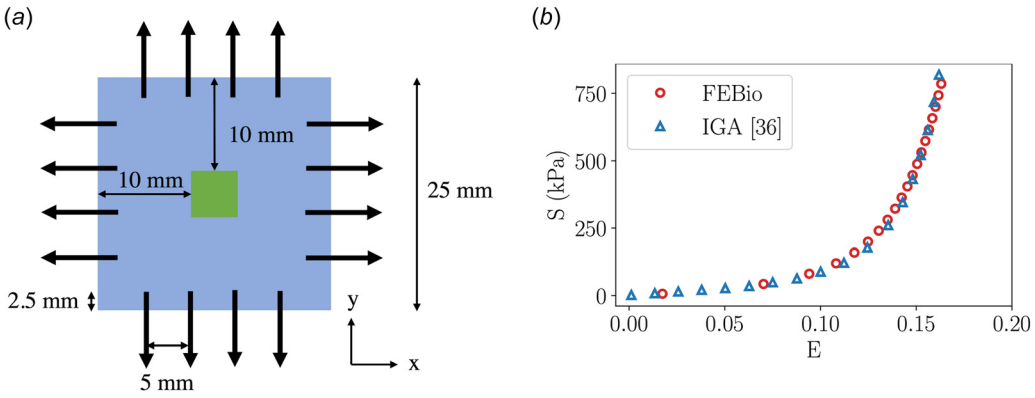

Fig. 14 Biaxial testing setup: (*a*) The geometry and loading condition of the square specimen. The black arrows are spaced 5 mm apart on each edge and indicate the direction of the applied loads. A 2.5 N nodal force was applied at the starting point of each arrow. The 5 mm by 5 mm green patch situated at the center of the specimen denotes the region of interest (ROI) for the stress and strain response. (*b*) The mean stress and strain curve in the x-direction at the ROI. FEBio's approximation displays excellent alignment compared with IGA approximation. Note: stress and strain in the y-direction were identical to those in the x-direction.

Appendix B: Additional Verification Results

Here, we report on additional stress and strain data for the mitral and tricuspid FE models.

Table 4 1st principal stresses and strains on the mitral valve with the fine mesh

	1st principal stress			1st principal strain		
	Mean	75th percentile	95th percentile	mean	75th percentile	95th percentile
Mitral	252.29	336.45	546.22	0.21	0.25	0.34
A1	489.89	572.02	635.20	0.31	0.35	0.38
A2	474.85	504.18	536.16	0.27	0.29	0.32
A3	522.06	566.63	618.20	0.31	0.34	0.37
P1	244.96	260.34	276.73	0.22	0.23	0.25
P2	267.06	282.82	300.47	0.23	0.24	0.24
P3	248.22	264.90	276.13	0.21	0.23	0.25

We observed the highest 95th percentile 1st principal stress and strain in region A1.

Table 5 1st principal stresses and strains on the tricuspid valve with the fine mesh

	1st principal stress			1st principal strain		
	Mean	75th percentile	95th percentile	mean	75th percentile	95th percentile
Tricuspid	64.83	82.62	127.27	0.51	0.59	0.63
Anterior	75.53	101.44	142.88	0.52	0.61	0.64
Posterior	68.76	86.71	112.94	0.51	0.58	0.62
Septal	51.48	65.08	90.20	0.51	0.58	0.61

We observed the highest 95th percentile 1st principal stress and strain in the anterior leaflet.

Appendix C: FEBioUncertainSCI Sensitivity

Here, we report on the sensitivity of FEBioUncertainSCI to the polynomial order and random number generator (Figs. 15–18).

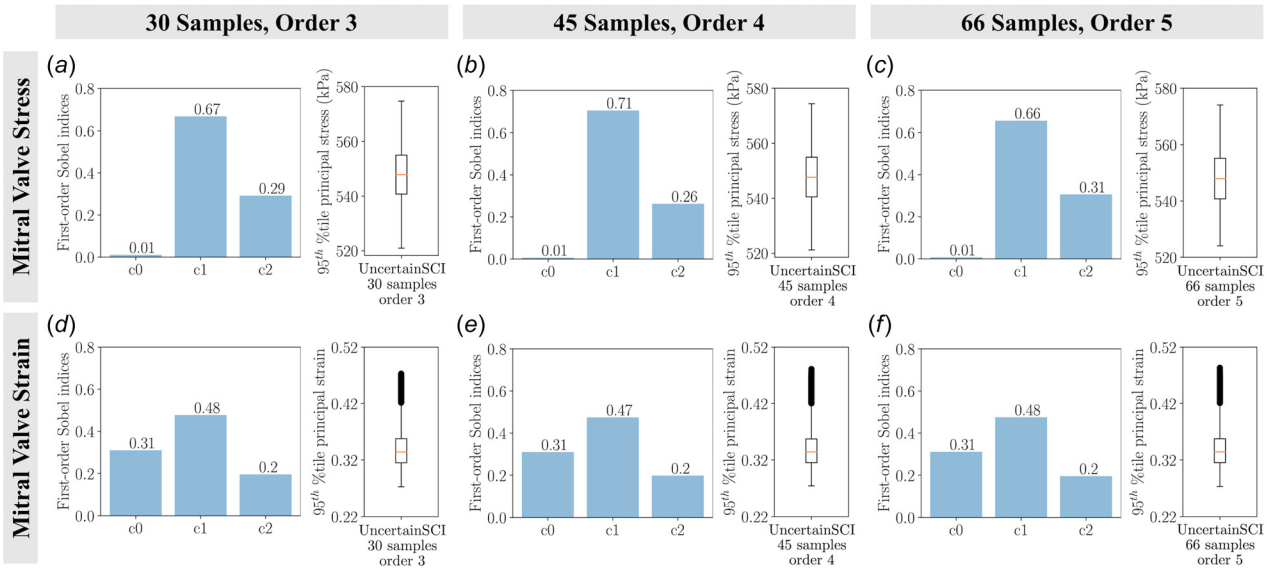

Fig. 15 The main sensitivity of the mitral valve stresses and strains as a function of material constants with varying polynomial chaos expansion (PCE) orders using UncertainSCI: (*a*) uncertainty in valve stress with 30 samples and PCE order 3, (*b*) uncertainty in valve stress with 45 samples and PCE order 4, (*c*) uncertainty in valve stress with 66 samples and PCE order 5, (*d*) uncertainty in valve strain with 30 samples and PCE order 3, (*e*) uncertainty in valve strain with 45 samples and PCE order 4, and (*f*) uncertainty in valve strain with 66 samples and PCE order 5. Bar plots denote the first-order Sobel indices and box plots depict the spread of stresses and strains of UncertainSCI samples with a fixed random seed of 0. We did not observe significant differences in the first-order Sobel indices.

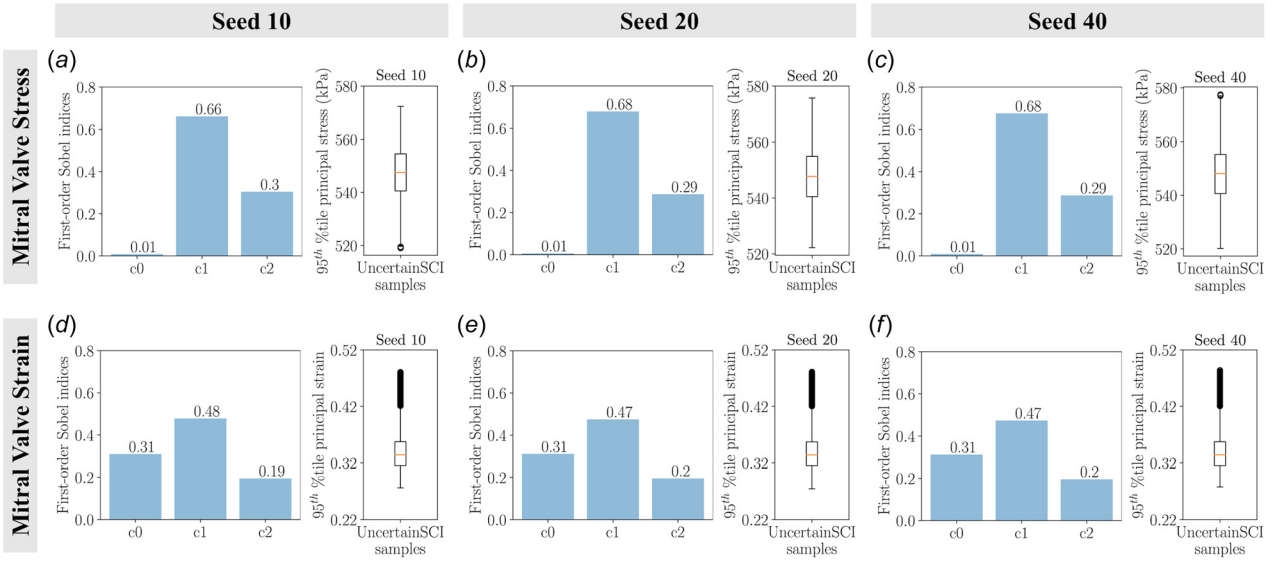

Fig. 16 The main sensitivity of the mitral valve stresses and strains as a function of material constants with varying random number generator seeds using UncertainSCI: (*a*) uncertainty in valve stress with random seed 10, (*b*) uncertainty in valve stress with random seed 20, (*c*) uncertainty in valve stress with random seed 40, (*d*) uncertainty in valve strain with random seed 10, (*e*) uncertainty in valve strain with random seed 20, and (*f*) uncertainty in valve strain with random seed 40. Bar plots denote the first-order Sobel indices and box plots depict the spread of stresses and strains of 45 UncertainSCI samples with fixed polynomial chaos expansion order 4. We did not observe significant differences in the first-order Sobel indices.

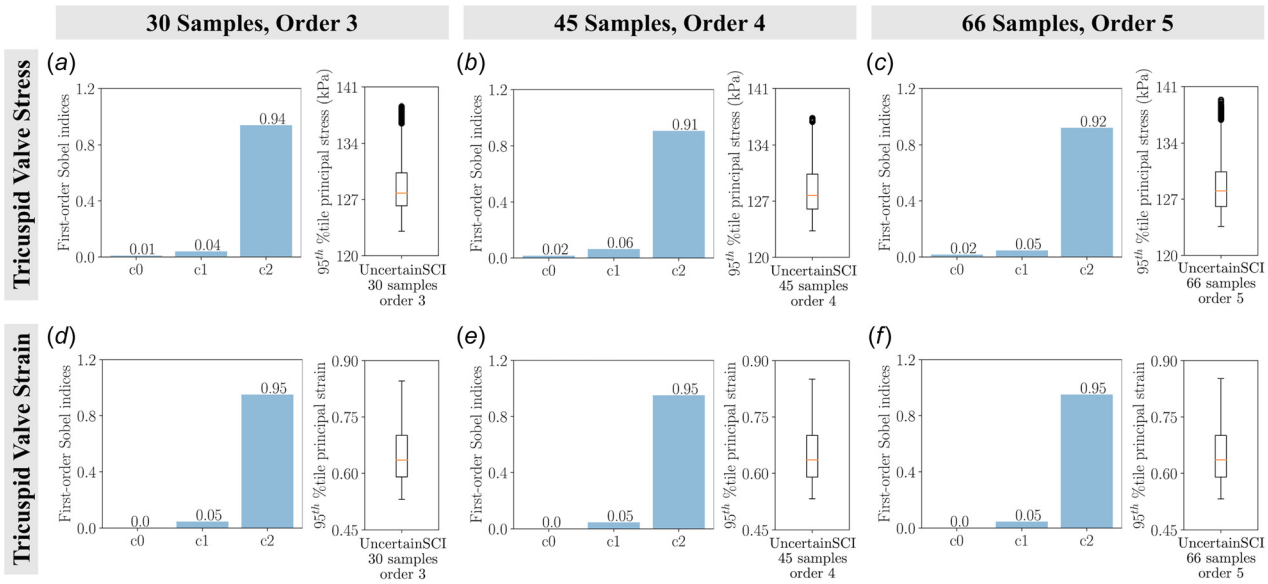

Fig. 17 The main sensitivity of the tricuspid valve stresses and strains as a function of material constants with varying polynomial chaos expansion (PCE) orders using UncertainSCI: (*a*) uncertainty in valve stress with 30 samples and PCE order 3, (*b*) uncertainty in valve stress with 45 samples and PCE order 4, (*c*) uncertainty in valve stress with 66 samples and PCE order 5, (*d*) uncertainty in valve strain with 30 samples and PCE order 3, (*e*) uncertainty in valve strain with 45 samples and PCE order 4, and (*f*) uncertainty in valve strain with 66 samples and PCE order 5. Bar plots denote the first-order Sobel indices and box plots depict the spread of stresses and strains of UncertainSCI samples with a fixed random seed of 0. We did not observe significant differences in the first-order Sobel indices.

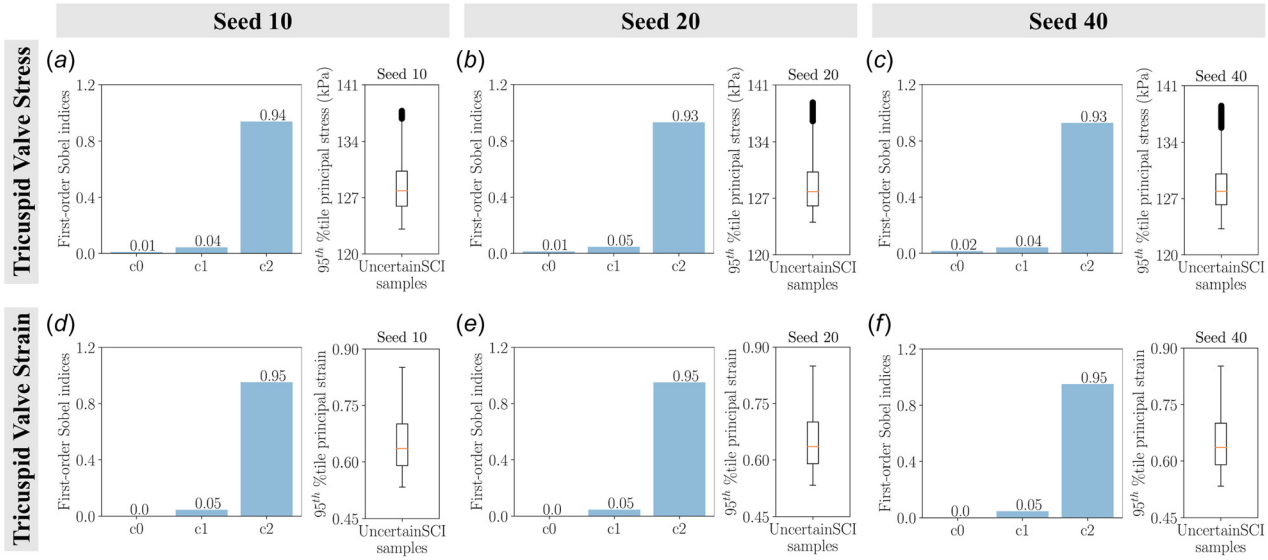

Fig. 18 The main sensitivity of the tricuspid valve stresses and strains as a function of material constants with varying random number generator seeds using UncertainSCI: (*a*) uncertainty in valve stress with random seed 10, (*b*) uncertainty in valve stress with random seed 20, (*c*) uncertainty in valve stress with random seed 40, (*d*) uncertainty in valve strain with random seed 10, (*e*) uncertainty in valve strain with random seed 20, and (*f*) uncertainty in valve strain with random seed 40. Bar plots denote the first-order Sobel indices and box plots depict the spread of stresses and strains of 45 UncertainSCI samples with fixed polynomial chaos expansion order 4. We did not observe significant differences in the first-order Sobel indices.

References

[1] Salgo, I. S., Gorman, J. H., Gorman, R. C., Jackson, B. M., Bowen, F. W., Plappert, T., St John Sutton, M. G., and Edmunds, L. H., 2002, "Effect of Annular Shape on Leaflet Curvature in Reducing Mitral Leaflet Stress," Circulation, **106**(6), pp. 711–717.

[2] Grewal, J., Suri, R., Mankad, S., Tanaka, A., Mahoney, D. W., Schaff, H. V., Miller, F. A., and Enriquez-Sarano, M., 2010, "Mitral Annular Dynamics in Myxomatous Valve Disease," Circulation, **121**(12), pp. 1423–1431.

[3] Levack, M. M., Jassar, A. S., Shang, E. K., Vergnat, M., Woo, Y. J., Acker, M. A., Jackson, B. M., Gorman, J. H., and Gorman, R. C., 2012, "Three-Dimensional Echocardiographic Analysis of Mitral Annular Dynamics," Circulation, **126**(11_suppl_1), pp. S183–S188.

[4] Lee, C. H., Oomen, P. J., Rabbah, J. P., Yoganathan, A., Gorman, R. C., Gorman, J. H., Amini, R., and Sacks, M. S., 2013, "A High-Fidelity and Micro-Anatomically Accurate 3D Finite Element Model for Simulations of Functional Mitral Valve," LNCS, **7945**, pp. 416–424.

[5] Kong, F., Pham, T., Martin, C., McKay, R., Primiano, C., Hashim, S., Kodali, S., and Sun, W., 2018, "Finite Element Analysis of Tricuspid Valve Deformation From Multi-Slice Computed Tomography Images," Ann. Biomed. Eng., **46**(8), pp. 1112–1127.

[6] Villard, P. F., Hammer, P. E., Perrin, D. P., del Nido, P. J., and Howe, R. D., 2018, "Fast Image-Based Mitral Valve Simulation From Individualized Geometry," Int. J. Medical Rob. Comput. Assisted Surg., **14**(2), p. 4.

[7] Biffi, B., Gritti, M., Grasso, A., Milano, E. G., Fontana, M., Alkareef, H., Davar, J., et al., 2019, "A Workflow for Patient-Specific Fluid–Structure Interaction Analysis of the Mitral Valve: A Proof of Concept on a Mitral Regurgitation Case," Medical Eng. Phys., **74**(12), pp. 153–161.

[8] Khalighi, A. H., Rego, B. V., Drach, A., Gorman, R. C., Gorman, J. H., and Sacks, M. S., 2019, "Development of a Functionally Equivalent Model of the Mitral Valve Chordae Tendineae Through Topology Optimization," Ann. Biomed. Eng., **47**(1), pp. 60–74.

[9] Sacks, M. S., Drach, A., Lee, C. H., Khalighi, A. H., Rego, B. V., Zhang, W., Ayoub, S., Yoganathan, A. P., Gorman, R. C., and Gorman, J. H., 2019, "On the Simulation of Mitral Valve Function in Health, Disease, and Treatment," ASME J. Biomech. Eng., **141**(7), p. 070804.

[10] Kong, F., Caballero, A., McKay, R., and Sun, W., 2020, "Finite Element Analysis of Mitraclip Procedure on a Patient- Specific Model With Functional Mitral Regurgitation," J. Biomech., **104**, p. 109730.

[11] Lee, C. H., Amini, R., Gorman, R. C., Gorman, J. H., and Sacks, M. S., 2014, "An Inverse Modeling Approach for Stress Estimation in Mitral Valve Anterior Leaflet Valvuloplasty for In-Vivo Valvular Biomaterial Assessment," J. Biomech., **47**(9), pp. 2055–2063.

[12] Khalighi, A. H., Drach, A., Bloodworth, C. H., Pierce, E. L., Yoganathan, A. P., Gorman, R. C., Gorman, J. H., and Sacks, M. S., 2017, "Mitral Valve Chordae Tendineae: Topological and Geometrical Characterization," Ann. Biomed. Eng., **45**(2), pp. 378–393.

[13] Kamensky, D., Xu, F., Lee, C. H., Yan, J., Bazilevs, Y., and Hsu, M. C., 2018, "A Contact Formulation Based on a Volumetric Potential: Application to Isogeometric Simulations of Atrioventricular Valves," Comput. Methods Appl. Mech. Eng., **330**(3), pp. 522–546.

[14] Singh-Gryzbon, S., Sadri, V., Toma, M., Pierce, E. L., Wei, Z. A., and Yoganathan, A. P., 2019, "Development of a Computational Method for Simulating Tricuspid Valve Dynamics," Ann. Biomed. Eng., **47**(6), pp. 1422–1434.

[15] Drach, A., Khalighi, A. H., and Sacks, M. S., 2018, "A Comprehensive Pipeline for Multi-Resolution Modeling of the Mitral Valve: Validation, Computational Efficiency, and Predictive Capability," Int. J. Numer. Methods Biomed. Eng., **34**(2), p. e2921.

[16] Lee, C. H., Rabbah, J. P., Yoganathan, A. P., Gorman, R. C., Gorman, J. H., and Sacks, M. S., 2015, "On the Effects of Leaflet Microstructure and Constitutive Model on the Closing Behavior of the Mitral Valve," Biomech. Model. Mechanobiol., **14**(6), pp. 1281–1302.

[17] Lee, C. H., Laurence, D. W., Ross, C. J., Kramer, K. E., Babu, A. R., Johnson, E. L., Hsu, M. C., et al., 2019, Mechanics of the Tricuspid Valve—From Clinical Diagnosis/Treatment, In-Vivo and In-Vitro Investigations, to Patient-Specific Biomechanical Modeling, Bioengineering, **6**(2), p. 47.

[18] Johnson, E. L., Laurence, D. W., Xu, F., Crisp, C. E., Mir, A., Burkhart, H. M., Lee, C. H., and Hsu, M. C., 2021, "Parameterization, Geometric Modeling, and Isogeometric Analysis of Tricuspid Valves," Comput. Methods Appl. Mech. Eng., **384**, p. 113960.

[19] Oomen, P. J. A., Holland, M. A., Bouten, C. V. C., Kuhl, E., and Loerakker, S., 2018, "Growth and Remodeling Play Opposing Roles During Postnatal Human Heart Valve Development," Sci. Rep., **8**(1), p. 1235.

[20] Rausch, M. K., 2020, "Growth and Remodeling of Atrioventricular Heart Valves: A Potential Target for Pharmacological Treatment?," Curr. Opin. Biomed. Eng., **15**, pp. 10–15.

[21] Kodigepalli, K. M., Thatcher, K., West, T., Howsmon, D. P., Schoen, F. J., Sacks, M. S., Breuer, C. K., and Lincoln, J., 2020, "Biology and Biomechanics of the Heart Valve Extracellular Matrix," J. Cardiovasc. Develop. Dis., **7**(4), p. 57.

[22] Kruithof, B. P. T., Paardekooper, L., Hiemstra, Y. L., Goumans, M.-J., Palmen, M., Delgado, V., Klautz, R. J. M., and Ajmone Marsan, N., 2019, "Stress-Induced Remodelling of the Mitral Valve: A Model for Leaflet Thickening and Superimposed Tissue Formation in Mitral Valve Disease," Cardiovasc. Res., **116**(5), pp. 931–943.

[23] Markby, G. R., Macrae, V. E., Summers, K. M., and Corcoran, B. M., 2020, "Disease Severity-Associated Gene Expression in Canine Myxomatous Mitral Valve Disease is Dominated by TGFβ Signaling," Front. Genet., **11**, p. 372.

[24] Maas, S. A., Ellis, B. J., Ateshian, G. A., and Weiss, J. A., 2012, "Febio: Finite Elements for Biomechanics," ASME J. Biomech. Eng., **134**(1), p. 011005.

[25] Maas, S. A., Ateshian, G. A., and Weiss, J. A., 2017, "Febio: History and Advances," Annu. Rev. Biomed. Eng., **19**(1), pp. 279–299.

[26] Ateshian, G. A., Shim, J. J., Maas, S. A., and Weiss, J. A., 2018, "Finite Element Framework for Computational Fluid Dynamics in Febio," ASME J. Biomech. Eng., **140**(2), p. 021001.

[27] Scanlan, A. B., Nguyen, A. V., Ilina, A., Lasso, A., Cripe, L., Jegatheeswaran, A., Silvestro, E., et al., 2018, "Comparison of 3D Echocardiogram-Derived 3D Printed Valve Models to Molded Models for Simulated Repair of Pediatric Atrioventricular Valves," Pediatric Cardiol., **39**(3), pp. 538–547.

[28] Nguyen, A. V., Lasso, A., Nam, H. H., Faerber, J., Aly, A. H., Pouch, A. M., Scanlan, A. B., et al., 2019, "Dynamic Three-Dimensional Geometry of the Tricuspid Valve Annulus in Hypoplastic Left Heart Syndrome With a Fontan Circulation," J. Am. Soc. Echocardiogr., **32**(5), pp. 655–666.

[29] Fedorov, A., Beichel, R., Kalpathy-Cramer, J., Finet, J., Fillion-Robin, J.-C., Pujol, S., Bauer, C., et al., 2012, "3D Slicer as an Image Computing Platform for the Quantitative Imaging Network," Magn. Reson. Imaging, **30**(9), pp. 1323–1341.

[30] Herz, C., Cianciulli, A., Ching, S., Vigil, C., Lasso, A., Nam, H. H., Drouin, S., et al., 2021, "Open-Source Tool Kit for Interactive Planning of Transcatheter Mitral Valve Replacement Using Multimodality Imaging," J. Am. Soc. Echocardiogr., **34**(8), pp. 917–920.

[31] Sacks, M. S., David Merryman, W., and Schmidt, D. E., 2009, "On the Biomechanics of Heart Valve Function," J. Biomech., **42**(12), pp. 1804–1824.

[32] Maxfield, M. W., Cleary, M. A., and Breuer, C. K., 2014, "Chapter 40 - Tissue-Engineering Heart Valves," *Principles of Tissue Engineering*, R. Lanza, R. Langer, and J. Vacanti, eds., 4th ed., Academic Press, Boston, MA, pp. 813–833.

[33] Jett, S., Laurence, D., Kunkel, R., Babu, A. R., Kramer, K., Baumwart, R., Towner, R., Wu, Y., and Lee, C.-H., 2018, "An Investigation of the Anisotropic Mechanical Properties and Anatomical Structure of Porcine Atrioventricular Heart Valves," J. Mech. Behav. Biomed. Mater., **87**, pp. 155–171.

[34] Hudson, L. T., Jett, S. V., Kramer, K. E., Laurence, D. W., Ross, C. J., Towner, R. A., Baumwart, R., et al., 2020, "A Pilot Study on Linking Tissue Mechanics With Load-Dependent Collagen Microstructures in Porcine Tricuspid Valve Leaflets," Bioengineering, **7**(2), p. 60.

[35] Meador, W. D., Mathur, M., Sugerman, G. P., Jazwiec, T., Malinowski, M., Bersi, M. R., Timek, T. A., and Rausch, M. K., 2020, "A Detailed Mechanical and Microstructural Analysis of Ovine Tricuspid Valve Leaflets," Acta Biomat., **102**, pp. 100–113.

[36] Wu, M. C., Zakerzadeh, R., Kamensky, D., Kiendl, J., Sacks, M. S., and Hsu, M. C., 2018, "An Anisotropic Constitutive Model for Immersogeometric Fluid–Structure Interaction Analysis of Bioprosthetic Heart Valves," J. Biomech., **74**(6), pp. 23–31.

[37] Hou, J. C., Maas, S. A., Weiss, J. A., and Ateshian, G. A., 2018, "Finite Element Formulation of Multiphasic Shell Elements for Cell Mechanics Analyses in Febio," ASME J. Biomech. Eng., **140**(12), p. 121009.

[38] Stevanella, M., Votta, E., Lemma, M., Antona, C., and Redaelli, A., 2010, "Finite Element Modelling of the Tricuspid Valve: A Preliminary Study," Med. Eng. Phys., **32**(10), pp. 1213–1223.

[39] Burk, K. M., Narayan, A., and Orr, J. A., 2020, "Efficient Sampling for Polynomial Chaos-Based Uncertainty Quantification and Sensitivity Analysis Using Weighted Approximate Fekete Points," Int. J. Numer. Methods Biomed. Eng., **36**(11), p. e3395.

[40] Becker, W., Rowson, J., Oakley, J. E., Yoxall, A., Manson, G., and Worden, K., 2011, "Bayesian Sensitivity Analysis of a Model of the Aortic Valve," J. Biomech., **44**(8), pp. 1499–1506.

[41] Mansi, T., Voigt, I., Georgescu, B., Zheng, X., Mengue, E. A., Hackl, M., Ionasec, R. I., Noack, T., Seeburger, J., and Comaniciu, D., 2012, "An Integrated Framework for Finite-Element Modeling of Mitral Valve Biomechanics From Medical Images: Application to Mitralclip Intervention Planning," Med. Image Anal., **16**(7), pp. 1330–1346. 10

[42] Grbic, S., Easley, T. F., Mansi, T., Bloodworth, C. H., Pierce, E. L., Voigt, I., Neumann, D., et al., 2017, "Personalized Mitral Valve Closure Computation and Uncertainty Analysis From 3D Echocardiography," Medical Image Anal., **35**(1), pp. 238–249.

[43] Narang, H., Rego, B. V., Khalighi, A. H., Aly, A., Pouch, A. M., Gorman, R. C., Gorman, J. H., III,., and Sacks, M. S., 2021, "Pre-Surgical Prediction of Ischemic Mitral Regurgitation Recurrence Using In vivo Mitral Valve Leaflet Strains," Ann. Biomed. Eng., **49**(12), pp. 3711–3723.

[44] Votta, E., Caiani, E., Veronesi, F., Soncini, M., Montevecchi, F. M., and Redaelli, A., 2008, "Mitral Valve Finite-Element Modelling From Ultrasound Data: A Pilot Study for a New Approach to Understand Mitral Function and Clinical Scenarios," Philos. Trans. R. Soc. A: Math., Phys. Eng. Sci., **366**(1879), pp. 3411–3434.

[45] Wang, Q., and Sun, W., 2013, "Finite Element Modeling of Mitral Valve Dynamic Deformation Using Patient-Specific Multi-Slices Computed Tomography Scans," Ann. Biomed. Eng., **41**(1), pp. 142–153.

[46] Rausch, M. K., Bothe, W., Kvitting, J., Göktepe, S., Craig Miller, D., and Kuhl, E., 2011, "In vivo Dynamic Strains of the Ovine Anterior Mitral Valve Leaflet," J. Biomech., **44**(6), pp. 1149–1157.

[47] El-Tallawi, K. C., Zhang, P., Azencott, R., He, J., Herrera, E. L., Xu, J., Chamsi-Pasha, M., Jacob, J., Lawrie, G. M., and Zoghbi, W. A., 2021, "Valve Strain Quantitation in Normal Mitral Valves and Mitral Prolapse With Variable Degrees of Regurgitation," JACC: Cardiovasc. Imag., **14**(6), pp. 1099–1109.

[48] Laurence, D. W., Johnson, E. L., Hsu, M. C., Baumwart, R., Mir, A., Burkhart, H. M., Holzapfel, G. A., Wu, Y., and Lee, C. H., 2020, "A Pilot in Silico Modeling-Based Study of the Pathological Effects on the Biomechanical Function of Tricuspid Valves," Int. J. Numer. Methods Biomed. Eng., **36**(7), p. 7.
[49] Mathur, M., Jazwiec, T., Meador, W. D., Malinowski, M., Goehler, M., Ferguson, H., Timek, T. A., and Rausch, M. K., 2019, "Tricuspid Valve Leaflet Strains in the Beating Ovine Heart," Biomech. Model. Mechanobiol., **18**(10), pp. 1351–1361.
[50] Jimenez, J. H., Soerensen, D. D., He, Z., Ritchie, J., and Yoganathan, A. P., 2005, "Mitral Valve Function and Chordal Force Distribution Using a Flexible Annulus Model: An In vitro Study," Ann. Biomed. Eng., **33**(5), pp. 557–566.
[51] Prot, V., Haaverstad, R., and Skallerud, B., 2009, "Finite Element Analysis of the Mitral Apparatus: Annulus Shape Effect and Chordal Force Distribution," Biomech. Model. Mechanobiol., **8**(1), pp. 43–55.
[52] Kamensky, D., Hsu, M.-C., Schillinger, D., Evans, J. A., Aggarwal, A., Bazilevs, Y., Sacks, M. S., and Hughes, T. J., 2015, "An Immersogeometric Variational Framework for Fluid–Structure Interaction: Application to Bioprosthetic Heart Valves," Comput. Methods Appl. Mech. Eng., **284**, pp. 1005–1053.
[53] Aggarwal, A., and Sacks, M. S., 2016, "An Inverse Modeling Approach for Semilunar Heart Valve Leaflet Mechanics: Exploitation of Tissue Structure," Biomech. Model. Mechanobiol., **15**(4), pp. 909–932.
[54] Morganti, S., Auricchio, F., Benson, D., Gambarin, F., Hartmann, S., Hughes, T., and Reali, A., 2015, "Patient-Specific Isogeometric Structural Analysis of Aortic Valve Closure," Comput. Methods Appl. Mech. Eng., **284**, pp. 508–520.
[55] Rupp, L. C., Liu, Z., Bergquist, J. A., Rampersad, S., White, D., Tate, J. D., Brooks, D. H., Narayan, A., and MacLeod, R. S., 2020, "Using Uncertainsci to Quantify Uncertainty in Cardiac Simulations," Computing in Cardiology, Rimini, Italy, Sept. 13–16, pp. 1–4.
[56] Pham, T., Kong, F., Martin, C., Wang, Q., Primiano, C., McKay, R., Elefteriades, J., and Sun, W., 2017, "Finite Element Analysis of Patient-Specific Mitral Valve With Mitral Regurgitation," Cardiovasc. Eng. Technol., **8**(1), pp. 3–16.
[57] Kong, F., Pham, T., Martin, C., Elefteriades, J., McKay, R., Primiano, C., and Sun, W., 2018, "Finite Element Analysis of Annuloplasty and Papillary Muscle Relocation on a Patient-Specific Mitral Regurgitation Model," PLoS ONE, **13**(6), p. e0198331.
[58] Martin, C., and Sun, W., 2012, "Biomechanical Characterization of Aortic Valve Tissue in Humans and Common Animal Models," J. Biomed. Mater. Res. Part A, **100A**(6), pp. 1591–1599.
[59] Pham, T., Sulejmani, F., Shin, E., Wang, D., and Sun, W., 2017, "Quantification and Comparison of the Mechanical Properties of Four Human Cardiac Valves," Acta Biomater., **54**, pp. 345–355.
[60] Sun, W., and Sacks, M. S., 2005, "Finite Element Implementation of a Generalized Fung-Elastic Constitutive Model for Planar Soft Tissues," Biomech. Model. Mechanobiol., **4**(2–3), pp. 190–199.